skb.se

SKB R-25-02

ISSN 1402-3091

ID 2082943

August 2025

Estimating transmissivity field based on fracture geometric characteristics and validation through hydro-mechanical coupling experiments and numerical simulations

Task 10 of SKB Task Force GWFTS – Validation approaches for groundwater flow and transport modelling with discrete features

Tai-Tien Wang, Po-Kai Chen
National Taiwan University, Department of Civil Engineering

Tsai-Ping Lee
Taiwan Power Company

Keywords: Fracture, Groundwater flow, Modelling, Upscaling, Normal loading

This report is published on www.skb.se

Abstract

This report investigates the hydro-mechanical coupling effects on the fracture transmissivity through numerical simulations, using high-resolution geometric data and experimental results. The mechanical model, incorporating initial contact state and Young's modulus, calculates the aperture fields under different stress states, which is crucial for predicting transmissivity fields. The steady-state head field is modelled using the Laplace equation, with a head difference applied across the fracture. Results show that the predicted flow rate trends align with experimental results, with discrepancies of less than one order of magnitude. Uncertainty analysis is conducted by varying the initial contact state, revealing that a reasonable range of assumptions can account for the observed variability. Flow rates in both directions exhibit similar trends, despite the significant decrease in transmissivity and flow rate as normal stress increases. The results highlight the importance of precise geometric data and mechanical properties in fracture flow modelling.

Sammanfattning

I denna rapport undersöks de hydromekaniska kopplingseffekterna på spricktransmissivitet genom numeriska simuleringar, och med hjälp av högupplösta geometriska data samt experimentella resultat. Den mekaniska modellen, som inkluderar initialt kontaktkvot och Youngs modul, beräknar den rumsliga aperturfördelningen under olika stresstillstånd, vilket är avgörande för att förutsäga transmissivitet. Tryckfördelningen i stationärt tillstånd modelleras med hjälp av en Laplace-ekvation, och med en tryckskillnad applicerad över sprickan. Resultaten visar att de predikterade flödestrenderna överensstämmer med experimentella resultat, med avvikelser på mindre än en storleksordning. Känslighetsanalysen påvisar att flödessimuleringsnätet uppnår massbevarande i stationärt tillstånd. Flödeshastigheter i båda riktningarna uppvisar liknande trender, trots den signifikanta minskningen i transmissivitet och flödeshastighet när lasten i normalriktingen ökar. Resultaten visar vikten av exakta geometriska data och mekaniska egenskaper i sprickflödesmodellering. Emellertid kan begränsningarna för att korrekt representera anisotropt beteende förbättras genom att justera transmissivitetsomvandlingsformeln för att uppnå bättre simuleringsresultat.

Content

1 Introduction 3
1.1 Background 3
1.2 Objectives 4
1.3 Scope 4

2 Description and objectives of Task 10.2.2 5
2.1 Objectives of Task 10.2.2 5
2.2 Limitation of Task 10.2.2 5
2.3 Data description 5
2.3.1 Phase 0: preparation of test sample 5
2.3.2 Phase 1: Hydromechanically coupled flow test on the unopened fracture 8
2.3.3 Phase 2 and 3: Measurements and testing of reassembled fracture sample and high normal load testing 15
2.3.4 Mechanical properties 18
2.4 Pragmatic validation 20

3 Modelling and methodology 21
3.1 Modelling tasks 21
3.1.1 Model purpose 21
3.1.2 Model description 21
3.1.3 Determination of critical aspects 22
3.1.4 Model parameters 22
3.1.5 Identification of influential factors 23
3.1.6 Uncertainty analyses 23
3.1.7 Workflow describing the modelling process 24
3.1.8 Pragmatic validation aspects 26
3.2 Prediction and validation of flow along a fracture at different normal loads 28
3.2.1 Definition of the performance measures and criteria 28
3.2.2 Task 10.2.2c: Prediction-outcome exercise of flow along an unopened fracture at different normal loads 28

4 Results 29
4.1 Geometrical characteristics 29
4.1.1 Roughness indices for entire fracture 29
4.1.2 Mechanical model and aperture field 32
4.1.3 Uncertainty Analysis of mechanical model 34
4.2 Water flow prediction 35
4.2.1 Flow rate prediction under various normal loads 35
4.2.2 Uncertainty analysis of hydraulic model 35
4.2.3 Minimum Transmissivity 35
4.2.4 Channelling effect under various normal loads 38

5 Discussion, summary, and conclusions 39
5.1 Discussion 39
5.2 Summary 41
5.3 Conclusions 41

References 42

1 Introduction

SKB Task Force on Modelling of Groundwater Flow and Transport of Solutes (Task 10 of the TF GWFTS) is dedicated to building confidence in and "validating" models of flow and transport in fractured rock. The objective is to develop pragmatic approaches to model validation within the Task Force. In addition to Task 10.1 "White Paper" (Lanyon et al. 2021), which sets out a possible development approach, Task 10.2 is the first of the Task 10 modelling tasks and focuses on the single fracture scale, with emphasis on in-fracture channelling.

Flow channelling in fractured rock is a phenomenon that occurs on different scales; and can have a range of safety-related implications. Channelling is for instance relevant to:

- Characterisation and interpretation of groundwater flow and transport in the host rock.
- Migration of meteoric water from the near-surface influences groundwater composition over long timescales due to interactions with subsurface geochemistry, density-driven flow, and transient hydrological changes.
- If a canister is damaged, radionuclides can be released into the groundwater system. Their migration is affected by flow conditions, matrix diffusion, sorption, and other retardation mechanisms.
- Inflows to deposition holes during buffer saturation and later flows around a deposition hole in the unlikely event of a breached canister.

In the contexts above, the channelling effect refers to the phenomenon where groundwater or solutes flow along preferential paths within fractures due to the asperity or heterogeneity in aperture field of the fractures. The channelled flow affects the pathways of groundwater movement and the transport of solutes, which has significant implications for the safe isolation of nuclear waste. Specifically, in fracture networks, channelled flow may accelerate solute migration and even impact the performance of barrier materials.

To characterize channelling, one often has only a limited amount of data. For instance, to investigate the suitability of a deposition hole on the meter scale, most likely only a single pilot borehole will be drilled, revealing that the flow rates measured in each intersected fracture can vary significantly on the centimetre to decimetre scale. Fracture mapping in the deposition tunnel could potentially yield additional information depending on the directions and extents of the fractures. Such observations would ideally give us estimates of the fracture surface topography and aperture field on the deposition hole scale. Note that the aperture field will be stress-dependent as well. Flow and transport in fractures or a fracture network depend on processes on a small scale that need to be "upscaled" in order to be used efficiently in larger-scale groundwater flow and mass transport models (Bruines, unpublished, and will be denoted solely Task Description in the following of this report)[1].

1.1 Background

National Taiwan University (abbreviated as NTU hereafter) participated in Task 10 as a modelling group since October 2022 (approximately one and half years later than other modelling groups). With the encouragement of other modelling groups participating in the 41st International Task Force GWFTS meeting held in Seoul, South Korea on April 18-20, 2023.

The participation of NTU as a modelling group is under the project entitled "Spent Nuclear Fuel Final Disposal Program: Technical Development Consulting and Parallel Verification of International Cases" supported by Taiwan Power Company (abbreviated as Tai-power hereafter). Major team members of NTU come from the Rock Mechanics Laboratory, Department of Civil Engineering RM/CE NTU. RM/CE NTU has studied the characteristics of rock joints since the 1990s.

[1] Bruines, P. SKB Task Force on Modelling of Groundwater Flow and Transport of Solutes: Description of Task 10.2. SKB R-23-10, Svensk Kärnbränslehantering AB, Stockholm, Sweden. Unpublished.

1.2 Objectives

The objectives of Task 10.2 are:

- Development of concepts and models for flow and transport at the single fracture scale.
- Consideration of the importance of hydro-mechanical coupling (normal loading only) on flow and transport.
- Development of modelling approaches for prediction of:
  - Flow and transport in single fractures.
  - Upscaled fracture properties from borehole to deposition hole scale.
- Building a starting point for pragmatic validation, i.e., a prediction-outcome exercise, as described in the white paper.

Task 10.2.1 is the first step in the road map for Task 10.2, focusing on geometrical evaluation of fracture surfaces and aperture field on a borehole scale and predicting fracture surface topography on the meter scale. Task 10.2.2 focuses on prediction of flow through a known fracture geometry at different normal loads, building a bridge to the possible objective of Task 10.2.3 which is suggested to predict transport through a known fracture geometry at different normal loads.

1.3 Scope

Based on the modelling exercises regarding geometrical evaluation of fracture surfaces and aperture field using four 100 x 70 mm^2 fractures carried out in Task 10.2.1, the NTU modelling team continues geometrical evaluation on a 200 x 200 mm^2 fracture, and then predicts flow through this known fracture geometry at different normal loads. An in-house developed software based on the finite difference concept is used. Factors that influence the water flow through the fracture will be discussed based on the modelled results.

2 Description and objectives of Task 10.2.2

In this subtask, the flow through a fracture under different normal loads will be investigated and modelled. The basic information provided in SKB Task Force on Modelling of Groundwater Flow and Transport of Solutes: the Task Description of Task 10.2 is summarized as follows.

2.1 Objectives of Task 10.2.2

The main objectives of this subtask are:

- Prediction and validation of the upscaled fracture geometry from borehole-sized fracture geometry and/or fracture trace geometry.
- Prediction and validation of flow along a fracture at different normal stresses.
- Support of the development and demonstration of pragmatic validation workflow at the single fracture scale.

2.2 Limitation of Task 10.2.2

Fractures typically show a range of internal structures that depend on the conditions during and after their formation. These conditions include, among others, rock stress history, temperature, and geochemical evolution. One end member could be a fresh fracture formed under an extensional stress field. The other end member could be a network of multiple fractures often associated with various porosities including mineral precipitation, gouge, breccia, and rock alteration.

The fracture used for this subtask is a relatively clean vertical natural fracture retrieved at a relatively shallow depth that shows only limited mineral precipitation. Care should be taken when extrapolating conclusions to different types of fractures.

2.3 Data description

The data the Task Force provided are from a set of hydromechanically coupled flow tests performed at the Borås facilities of Research Institutes of Sweden (RISE) on a 20 x 20 x 25 cm^3 rock sample that includes a single “simple” natural fracture. The rock sample was obtained from the same location in the Flivik rock quarry and the fracture is believed to be parallel to, and of similar geological origin as the samples used in Task 10.2.1. The data from the rock sample have been gathered as part of an extension of the second phase of the POST project and have been provided by the POST project as a courtesy to the Task Force, including:

- geometrical data of the unopened and opened rock sample,
- contact pressure measurements using pressure sensitive film,
- results of the hydromechanically coupled flow tests carried out on the rock sample,
- intact rock properties from previous tests on the rock from the same location.

Table 2-1 lists the overview of the hydromechanically coupled flow test program carried out on the unopened fracture sample as well as the planned continuation. The geometrical data of this fracture sample and associated experimental results will be used in Task 10.2.2. Testing phases and steps related to the measured data are briefly described in the following subsections.

2.3.1 Phase 0: preparation of test sample

The rock sample used is cut from a 19.6 ton block obtained from the same part of the Flivik quarry where the fracture samples for Task 10.2.1 came from. The fractures used in Tasks 10.2.1 and 10.2.2 are thought to be from similarly oriented fractures, with a similar geological history, belonging to the same fracture set. Figure 2-1 shows the block with the fracture used in Task 10.2.2., called Block 19.6. This block has been further subdivided into smaller blocks. Figure 2-2 (left) shows the subblock 19.6.1.4, and Figure 2-2 (right) shows the 20 cm slab from which the final 200 x 200 x 250 mm^3 sample is cut. It should be noted that for all samples containing a fracture, great care has been taken to keep the fractures in their mated position, i.e., to not open or disturb the fractures.

To prevent the sample from opening during transport from the stonemasonry, a support system was glued to the sample (Figure 2-3).

Before testing, the outer surfaces of the rock sample, with glued supports still attached, were measured with the help of a Leica T-Probe or a Reflector, in combination with a Leica Absolute Tracker AT960. The laser tracker automatically tracks and records the position of either the reflector or the T-Probe. The reflector, which has a higher resolution with an accuracy of 10 microns, was used for the top and bottom surfaces of the sample. The T-Probe, which has an accuracy of 30 microns, was used for the sides of the sample.

Before the test, high-resolution photos have been taken of the four sides of the sample with the fracture trace. The composite pictures of the fracture trace include about 40 pixels per mm (Figure 2-4). Similar pictures could be obtained from borehole TV data, or smooth deposition hole walls, and can yield information about fracture asperity and aperture fields.

Table 2-1. Overview of HM coupled flow test program carried out on fracture sample simulated in Task 10.2.2

Phase 0: preparation of test sample
Preparation of a 200 x 200 x 250 mm^3 sample with a natural fracture
High-resolution measurement of the closed sample dimension before testing
High-resolution photography of the fracture trace from four sides
Phase 1: Measurement and testing of the intact fracture sample
Hydromechanical flow testing of fracture
In two perpendicular directions (from Face 2 to Face 4 and from Face 1 to Face 3)
Flow measurements at approximately 0, 1, 2, 4, 8, 4, 2, 1, 0 MPa normal loading
Staining tracer test at 0.09 MPa
High-resolution measurement of the closed sample dimensions after testing
Opening of sample
Description of the fracture surface and broken off material including high-resolution photography of fracture surfaces under regular and UV light conditions
High-resolution scanning of both fracture surfaces
Contact pressure-film measurements at 1 and 4 MPa normal loading with low and medium pressure film
Phase 2: Measurements and testing of reassembled fracture sample
High-resolution measurement of the reassembled sample dimensions before testing
Hydromechanical flow testing of fracture
In one direction (from Face 2 to Face 4)
Flow measurements at approximately 0, 1, 2, 4, 8, 4, 2, 1, 0 MPa normal loading for three cycles (after which no significant settlements occurred)
Phase 3: High normal load testing
Hydromechanical flow testing of fracture
In one direction only (from Face 2 to Face 4)
Flow measurements at approximately 10, 20, 30 and 40 MPa normal loading
Reopen fracture
Record fracture damage
Rescanning of fracture surfaces
More detailed geological description

Figure 2-1. *The block with a weight of 19.6 tons used in Task 10.2.2. The fractures are horizontally oriented in the picture but were originally vertically oriented in the rock mass along the grain plane.*

Figure 2-2. *(left) Block 19.6.1.4 from which the sample is cut. (right) Slab of 19.6.1.4 block from which the 200 x 200 x 250 mm^3 is cut from.*

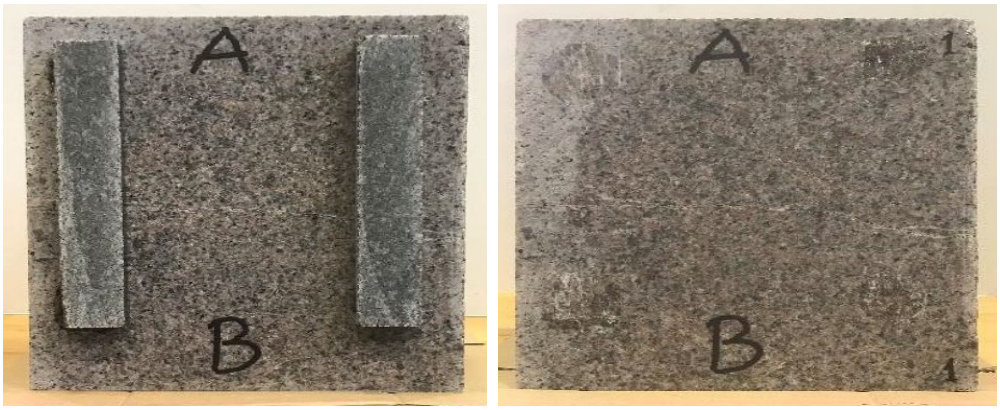

Figure 2-3. *Sample for hydromechanically coupled flow test with support for transport (left), and without support (right).*

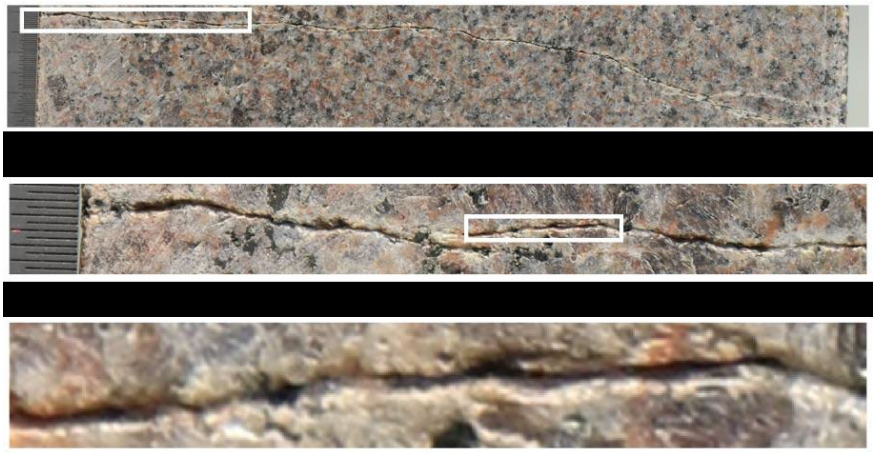

Figure 2-4. *Example of a high-resolution fracture trace photo.*

2.3.2 Phase 1: Hydromechanically coupled flow test on the unopened fracture

Figure 2-5 shows the schematic drawing of the most important components of the HM test. The basic principle of the test is to attach in- and outflow devices to opposite sides of the fracture, seal the sides of the fracture, place the sample, including instrumentations to capture both hydraulically and mechanically significant measurements, into a uniaxial test apparatus and measure flow rates through the fracture at different hydraulic gradients and normal stress conditions. For the test, regular tap water has been used. During the test, a normal compressive force, F, is applied to the rock sample. Any deformation, δ, over a section of the rock sample including the fracture is recorded. Water from the upper vessel, V1, with a water height H_{in}, is connected to the inflow box where it results in a pressure, P_{in}. On the outflow flow side, the outflow box is connected to a vessel V2 that includes an overflow. The height H_{out} results in a P_{out}, in the outflow box. The values P_{in} and P_{out} allow for a correct determination of the gradient over the fracture sample. The overflowing water is collected in vessel V3, where a load cell continuously measures the mass of the collected water, M_w. For a correct determination of the viscosity and density of the water during the test, the temperature is measured on the rock close to the inflow, T_r, and in the water in vessel V2, T_w.

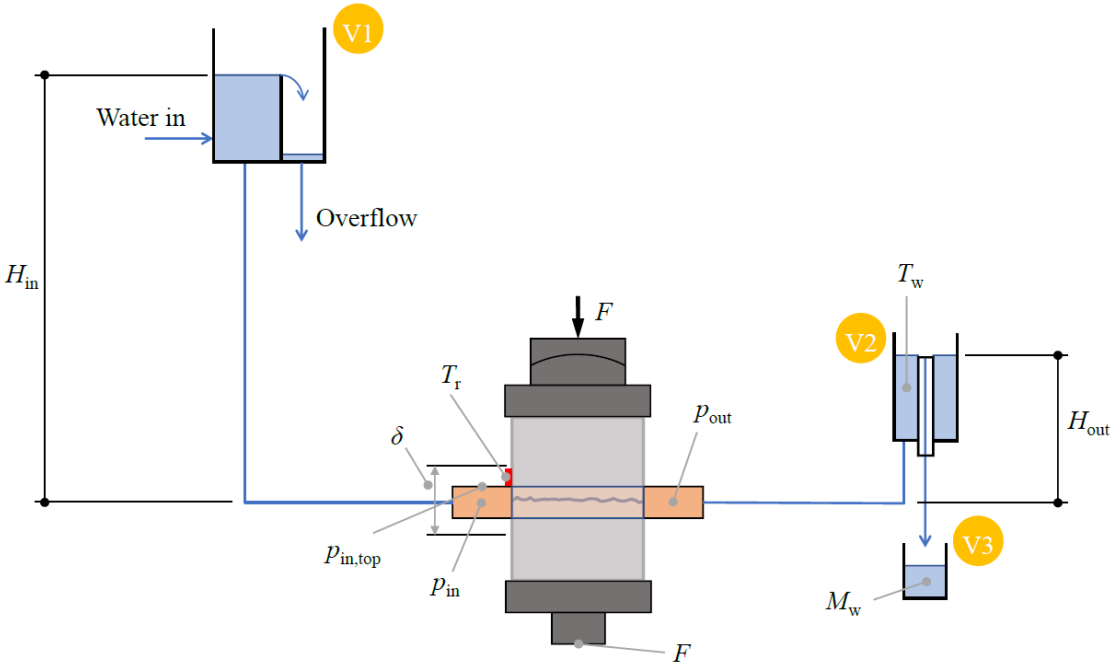

Figure 2-5. *Schematic drawing of the most important components of the HM test.*

Flow through the fracture is along the sample in two orthogonal directions. To achieve this, a rubber band with cut-out sections at the desired in and outflow sides of the fracture is placed around the rock sample and gasket sealant is applied (Figure 2-6a). On top of the cut-out sections, inflow and outflow boxes were placed. On the sides of the sample, side plates were installed. Using a frame, pressure was applied on all sides to make sure no significant water leakage occurred from any of the four sides of the sample. Figure 2-6b shows the complete hydraulic set-up for a leakage test before placement in the triaxial test machine. The hoses connected to the in- and outflow boxes are for supplying water to and from the fracture. The thinner blue tubes connect the hydraulic pressure gauges to determine the gradient over the fracture. Additionally, one temperature sensor is placed on the rock close to the inflow and one in the water in the overflow vessel on the outflow side. The temperature measurements can be used to correct for any temperature dependent changes in viscosity or density of the water.

To generate the hydraulic gradient, the inflow side was connected to a bucket filled with tap water that could be lifted to the desired height (Figure 2-7a). Outflow was measured by means of a high precision-load cell connected to the receptacle that catches the outflow from the fracture (Figure 2-7b). To obtain a regular dripping of water into the measurement receptacle, an overflow has been made from a Teflon tube in which a rounded notch was cut (Figure 2-7c).

To generate the normal stresses needed for the test, the sample is placed in the triaxial test apparatus (RTR – 150HS9 from GCTS) shown in Figure 2-8. Once the sample is placed in the triaxial machine, frames are attached to the top and bottom of the sample. On the four corners of this frame, miniature LVDTs (Linear Variable Differential Transformers) are placed. A schematic drawing of the LVDT locations can be seen in Figure 2-9. The length of the LVDTs (gauge length) was, respectively, 140 and 147 mm for the flow measurements before and after the opening of the fracture. The distance between the LVDTs are 200 mm and 320 mm, respectively, in the direction of flow and perpendicular to it. The actual LVDTs as installed are shown in Figure 2-10.

(a) (b)

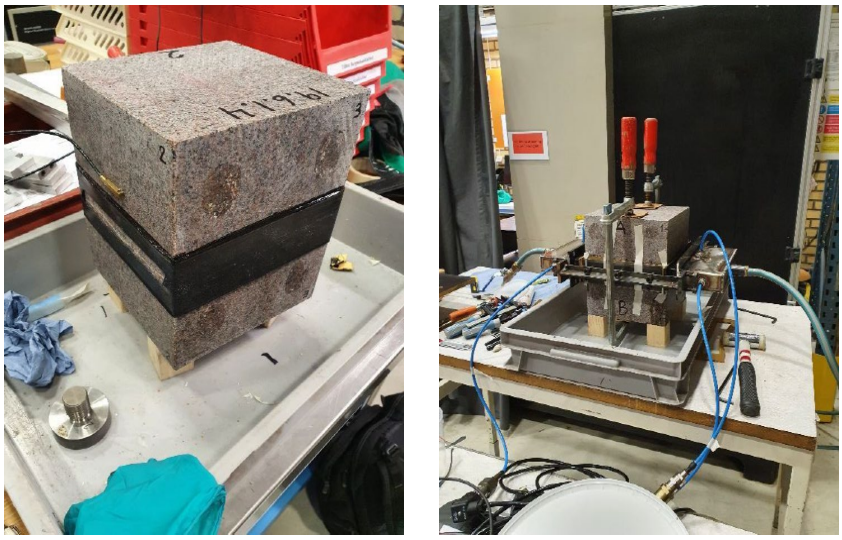

Figure 2-6. *Rock sample with rubber band placed over fracture and gasket sealant applied (a). Rock sample with installed inflow box and outflow box including instrumentation to measure hydraulic pressure and water temperature, as well as side plates installed to prevent water leakage from the sides of the sample (b).*

(a) (b) (c)

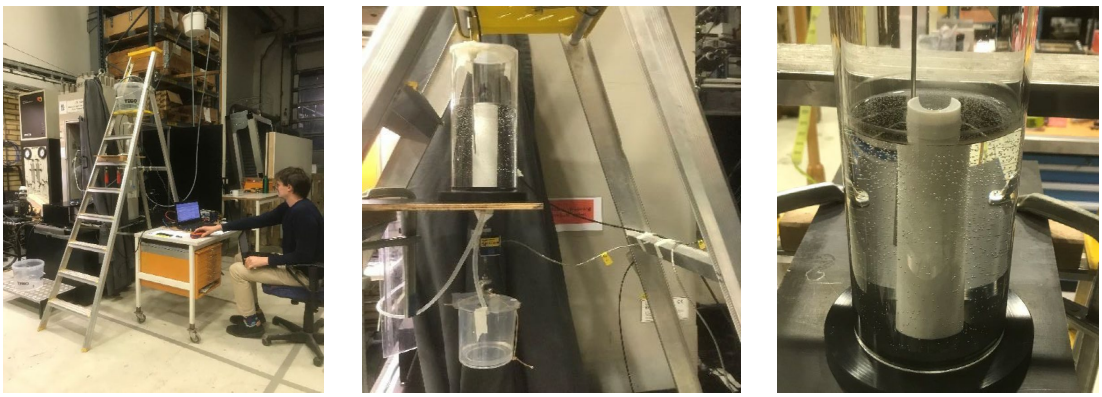

Figure 2-7. *(a) Overview of the entire test set up including white bucket (V1) supplying hydraulic gradient. (b) Measurement of overflow on the outflow side including the overflow vessel (V2) and the collection vessel (V3) using a high precision load cell. (c) Overflow vessel with Teflon overflow tube with notch.*

Figure 2-8. *Triaxial test apparatus, including controls, in which the sample is placed.*

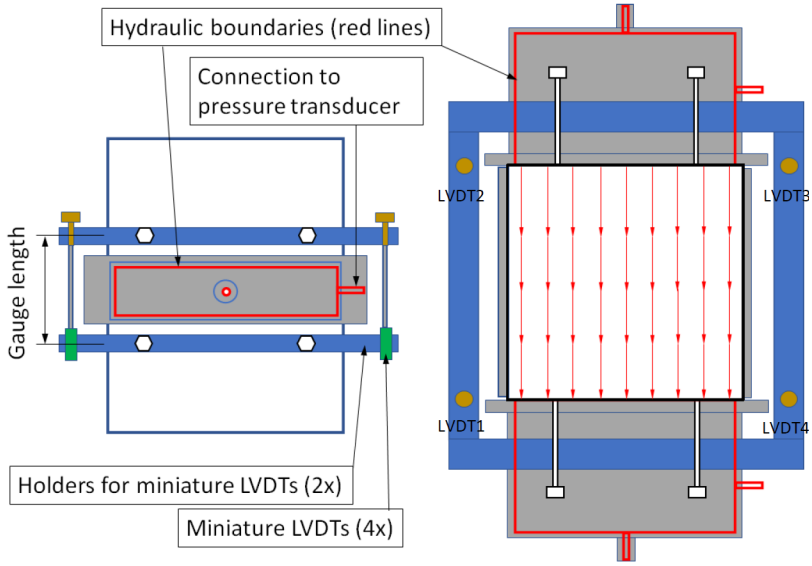

Figure 2-9. *Schematic drawing of the miniature LVDTs installed. The gauge length was 140 and 147 mm respectively for the flow tests before and after opening of the fracture. The distance between the LVDTs in the direction of flow is 200 mm (corresponding with the size of the rock sample). The distance between the LVDT perpendicular to the direction of flow is 320 mm.*

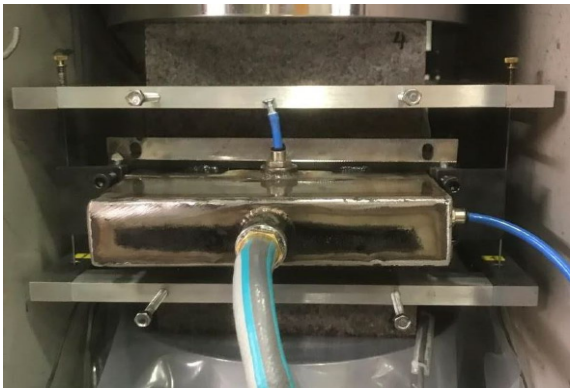

Figure 2-10. *Photograph of the set-up including the LVDTs. The two LVDTs on the outflow side are visible. The LVDTs are numbered clockwise. LVDT 1 is visible in the left and LVDT 4 is visible on the right.*

All instruments are connected to a computer and values are automatically logged. The main measurement values recorded are:

- Time (s)
- Pressures at in- and outlets (bar)
- Force at load cell of the outflow collection receptacle (N)
- Temperature of water and rock at inlet (°C)
- Displacements from 4 LVDTs (mm)
- Normal load applied by triaxial machine (kN)
- Flow rate (ml/s)

Table 2-2 and Table 2-3 show the main measurements and calculations from the HM tests in the unopened fracture in directions 2-4 and 1-3, respectively.

These tables include the spatial averaged normal stress (σ) applied to the fracture specimen based on applied force and the size of the specimen (200 x 200 mm^2), the displacement based on the average value of four LVDTs, the difference of hydraulic head (Δh) between the inflow and outflow boxes based on the measured spatial averaged hydraulic pressures (P_{in} and P_{out}), flow rate (Q) at outflow box, and equivalent transmissivity (T), which is calculated by ($T = \frac{Q}{\left(\frac{\Delta h}{w}\right)w}$), where w is specimen width 200 mm.

After the HM test, a Rhodamine-B tracer was flushed through the fracture. Rhodamine-B was selected as it sorbs well to rock. The concentration used was 0.1 mg/L. Figure 2-11 (a) shows the prepared tracer on the left. The direction of flow was from Face 1 to Face 3. The normal stress on the sample was 0.09 MPa due to the dead weight of the sample and loading plates. After opening, both upper and lower surfaces were photographed using two different UV light sources as well as different exposure times. Further treatment of the photographs (example in Figure 2-11 (b)) is needed to determine the flow wetted surfaces. Ideally, the staining would be used for verification of the modelled flow wetted surface.

The outside of the closed sample was measured again with the same methods described previously. This was done to see if the normal loading resulted in a change in the dimensions of the fracture sample. Using a best-fit approach, the grids before and after the HM testing of the unopened sample were compared. The measured deviations were between -0.034 mm and 0.026 mm. The average deviation was 0.003 mm. Figure 2-12 shows the difference between the two grids.

To measure the fracture surface, the fracture has to be opened. The fracture did not open spontaneously without force; therefore, a device as shown schematically in Figure 2-13 (a) was used to apply an additional force. The estimate is that about a 100 Nm moment was necessary to break the remaining rock bridges between the fracture surfaces.

As Figure 2-13b and 2-13c show, only a few slivers detached from the fracture walls. The topography and mineralogy of opened fracture surfaces were recorded in detail. Apart from some white coloured infill, that is believed to be calcite, no other mineralisation was visible. Detailed inspection showed that the resulting fracture followed grain boundaries. Only in a few parts does the fracture go through grains.

Table 2-2. Conditions under which the different HM tests have been carried out in the direction from Face 2 to Face 4

	σ (MPa)	LVDT_Ave. (mm)	Displacement (mm)	Viscosity (mPa-s)	Density (kg/m^3)	Δh (m)	Q (m^3/s)	T (m^2/s)
1	0.0	-6.0E-03	0.0	1.02	998.3	4.27	1.1E-07	2.6E-08
2	0.0	-4.4E-03	1.6E-03	1.02	998.3	3.76	8.8E-08	2.3E-08
3	0.0	-3.8E-03	2.1E-03	1.02	998.3	3.25	7.0E-08	2.2E-08
4	0.0	-3.6E-03	2.4E-03	1.02	998.3	2.74	5.4E-08	2.0E-08
5	0.0	-3.1E-03	2.9E-03	1.02	998.3	2.24	4.0E-08	1.8E-08
6	1.0	2.5E-03	8.5E-03	1.02	998.4	4.28	2.8E-08	6.4E-09
7	1.0	2.5E-03	8.5E-03	1.02	998.4	3.76	2.3E-08	6.1E-09
8	1.0	2.5E-03	8.5E-03	1.02	998.4	3.25	1.9E-08	5.7E-09
9	1.0	2.5E-03	8.5E-03	1.02	998.4	2.74	1.4E-08	5.2E-09
10	1.0	2.4E-03	8.4E-03	1.02	998.4	2.23	1.0E-08	4.6E-09
11	2.0	7.4E-03	1.3E-02	1.02	998.4	4.27	1.8E-08	4.2E-09
12	2.0	7.6E-03	1.4E-02	1.02	998.4	3.76	1.5E-08	3.9E-09
13	2.0	7.6E-03	1.4E-02	1.02	998.4	3.25	1.1E-08	3.4E-09
14	2.0	7.9E-03	1.4E-02	1.02	998.4	3.25	1.1E-08	3.4E-09
15	4.0	1.8E-02	2.4E-02	1.02	998.4	4.27	9.6E-09	2.2E-09
16	4.0	1.8E-02	2.4E-02	1.02	998.4	3.76	8.0E-09	2.1E-09
17	4.0	1.8E-02	2.4E-02	1.02	998.4	3.25	6.3E-09	1.9E-09
18	8.0	3.6E-02	4.2E-02	1.02	998.4	4.27	4.4E-09	1.0E-09
19	8.0	3.7E-02	4.3E-02	1.02	998.4	3.76	3.7E-09	9.8E-10
20	8.0	3.8E-02	4.4E-02	1.02	998.4	3.25	2.9E-09	8.9E-10
21	4.0	3.1E-02	3.7E-02	1.01	998.3	3.24	3.1E-09	9.6E-10
22	2.0	2.5E-02	3.1E-02	1.01	998.3	3.24	3.7E-09	1.1E-09
23	1.0	2.1E-02	2.7E-02	1.01	998.3	3.24	4.2E-09	1.3E-09
24	0.0	1.7E-03	7.7E-03	1.01	998.3	3.24	2.6E-08	7.9E-09

Table 2-3. Conditions under which the different HM tests have been carried out in the direction from Face 1 to Face 3

	σ	LVDT_Ave.	Displacement	Viscosity	Density	Δh	Q	T
	(MPa)	(mm)	(mm)	(mPa-s)	(kg/m^3)	(m)	(m^3/s)	(m^2/s)
1	0.0	-9.1E-03	0.0	1.02	998.4	4.29	1.6E-08	3.8E-09
2	0.0	-8.9E-03	2.3E-04	1.02	998.4	3.77	1.3E-08	3.4E-09
3	0.0	-8.8E-03	3.7E-04	1.02	998.4	3.26	9.6E-09	2.9E-09
4	1.0	-5.9E-03	3.2E-03	1.02	998.4	4.28	5.6E-09	1.3E-09
5	1.0	-5.6E-03	3.5E-03	1.02	998.4	3.77	4.3E-09	1.1E-09
6	1.0	-5.5E-03	3.6E-03	1.02	998.4	3.26	3.0E-09	9.2E-10
7	2.0	-9.2E-04	8.2E-03	1.02	998.4	4.28	3.3E-09	7.7E-10
8	2.0	-4.7E-04	8.6E-03	1.02	998.4	3.77	2.3E-09	6.1E-10
9	4.0	5.6E-03	1.5E-02	1.01	998.4	4.28	2.1E-09	4.9E-10
10	4.0	6.6E-03	1.6E-02	1.01	998.3	4.53	2.5E-09	5.5E-10
11	8.0	1.9E-02	2.8E-02	1.00	998.3	4.53	1.6E-09	3.5E-10
12	8.0	2.1E-02	3.0E-02	1.00	998.3	4.27	1.3E-09	3.0E-10
13	4.0	1.4E-02	2.3E-02	1.00	998.2	4.27	1.7E-09	4.0E-10
14	2.0	8.5E-03	1.8E-02	0.99	998.2	4.27	1.9E-09	4.4E-10
15	1.0	4.3E-03	1.3E-02	0.99	998.2	4.27	2.7E-09	6.3E-10
16	0.0	-1.2E-02	-2.9E-03	0.99	998.2	4.27	1.5E-08	3.4E-09

(a) (b)

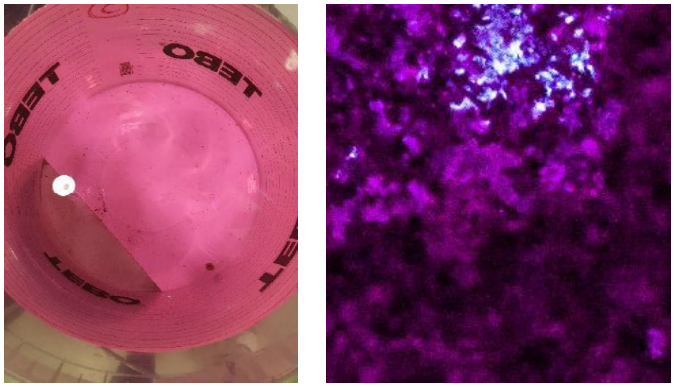

Figure 2-11. *(a) 10L bucket with Rhodamine-B tracer with a concentration of 0.1 mg/L seen from above. (b) Zoom in on a Rhodamine-B stained fracture surface.*

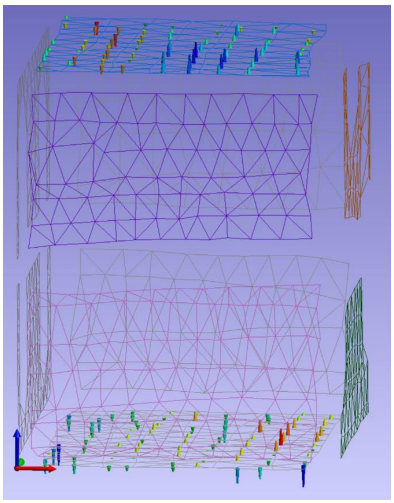

Figure 2-12. *Differences in the top and bottom surfaces of the rock sample as measured before and after HM testing of the unopened fracture sample.*

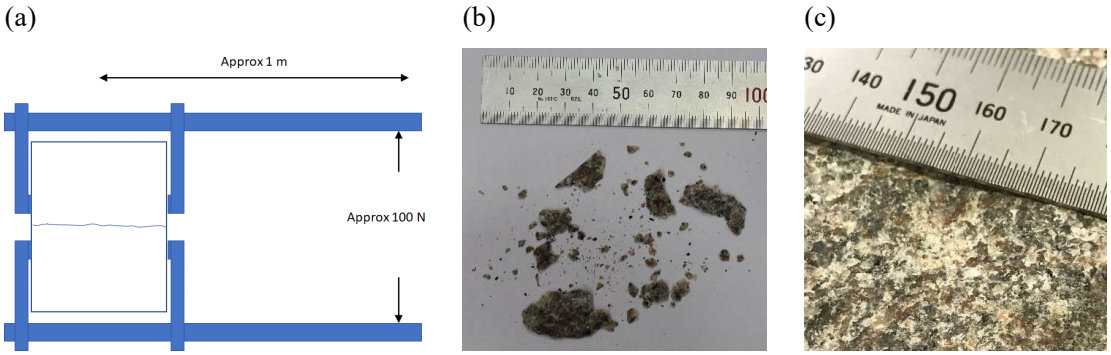

Figure 2-13. *(a) Device constructed to open the fracture sample. A rough estimate is that a 100N force was needed with the device that had about 1m leverage. (b) All rock slivers that detached during opening of the fracture sample, (c) Zoom in on fracture surface with what could be calcite fracture infill or coating.*

2.3.3 Phase 2 and 3: Measurements and testing of reassembled fracture sample and high normal load testing

After opening of the fracture, the upper and lower surfaces were scanned using a handheld laser scanner (Leica LAS) in combination with the Leica Absolute Tracker AT960. The precision of this system is reported by the supplier as 0.035 mm. The hand laser scan captures both the opened fracture surfaces and the sides of the sample. Using the higher precision outer surface measurements obtained with the Leica T-probe and Red Ring Reflectors, the laser scanned fracture surface data is referenced. The referenced, irregular surfaces are provided as ASCII.stl files. Each file is larger than 2GB. For convenience, also .csv versions of only the x, y, z coordinates of all nodes are provided. The resolution in the *x-y* plane (fracture surface) is approximately 0.1 to 0.2 mm. Figure 2-14 shows the top and bottom surfaces. Figure 2-15 shows the references top and bottom surfaces from all four sides. The description of Task 10.2 annotates that although great care has been taken to properly reference the top and bottom surfaces, additional fitting is most likely still necessary. A better fit is encouraged. The Task Force group is also working on better referencing the two surfaces. Once available, the Task Force can share such an improved referenced model.

Contact pressure film measurements have been carried out four times. The procedure is the same as used for the samples used in Task 10.2.1. Two different pressure film types have been used, a low pressure two-sheet type (PRESCALE LW) and a medium pressure mono-sheet type (PRESCALE MS). Both types have been used at two different normal stresses (1 and 4 MPa). Figure 2-16 shows the results of the contact pressure film measurements.

After reassembling the fracture, an HM test was conducted for water flow from Face 2 to Face 4. The test loading included repeated loading and unloading from 0 MPa to 8 MPa, and was further loaded up to 37.5 MPa. Table 2-4 shows the main measurements and calculations from the HM tests in the resealed fracture in directions 2-4 after opening of the fracture.

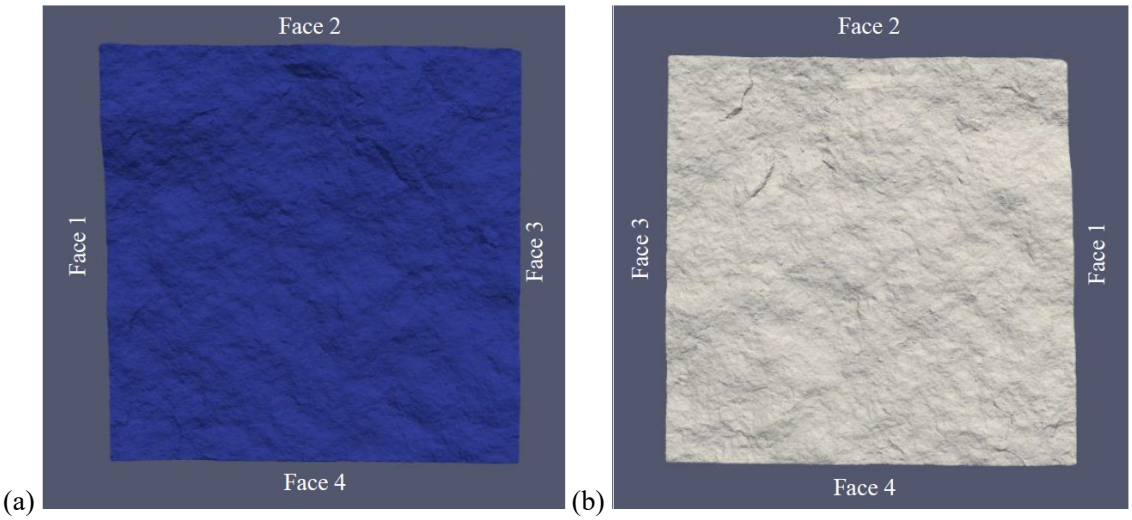

Figure 2-14. *(a) Upper surface seen from below, (b) lower surface seen from above.*

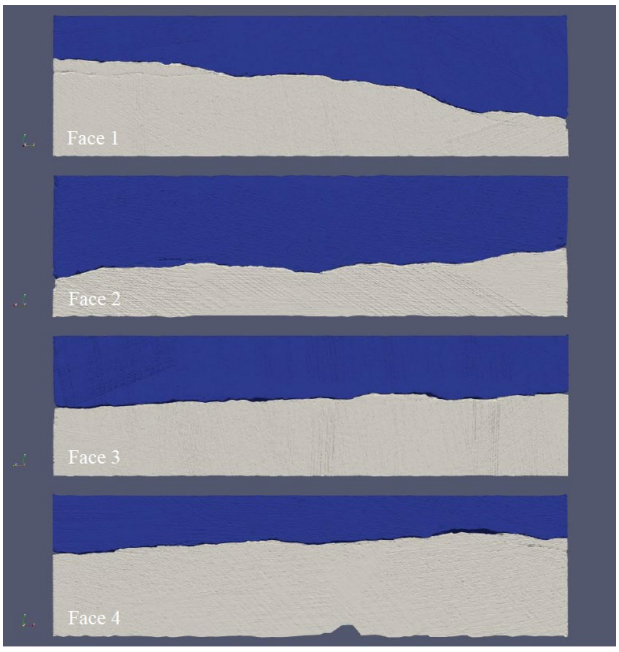

Figure 2-15. *Side view of the lower and upper surface from four different directions.*

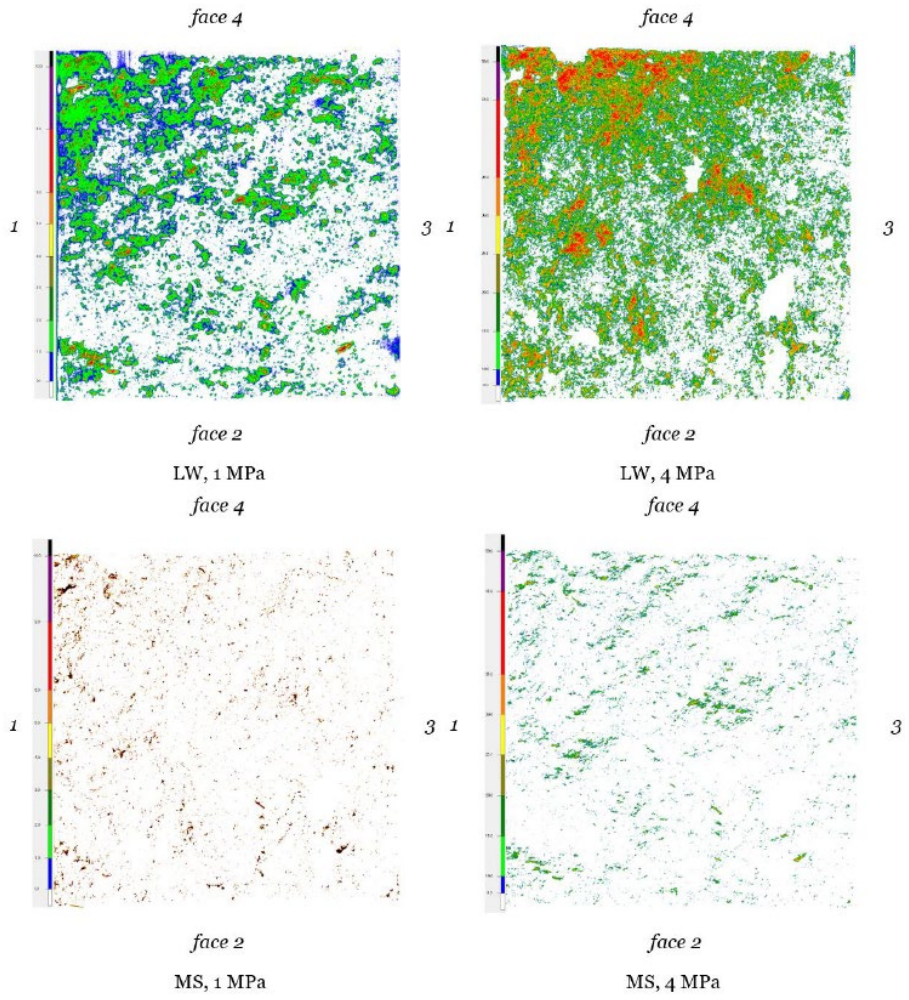

Figure 2-16. *Pressure film measurements showing local pressures in MPa for the fracture sample of: (upper left) low pressure film and normal stress of 1 MPa, (upper right) low pressure film and normal stress of 4 MPa, (lower left) medium pressure film and normal stress of 1 MPa, and (lower right) medium pressure film and normal stress of 4 MPa.*

Table 2-4. Conditions under which the different HM tests have been carried out in the direction from Face 2 to Face 4 with resealed fracture

	σ	LVDT_Ave.	Displacement	Viscosity	Density	Δh	Q	T
	(MPa)	(mm)	(mm)	(mPa-s)	(kg/m^3)	(m)	(m^3/s)	(m^2/s)
1	0.0	-2.1E-05	-4.1E-02	1.02	998.3	1.98	3.3E-07	1.7E-07
2	0.0	8.1E-04	-4.0E-02	1.02	998.3	1.46	2.0E-07	1.4E-07
3	0.0	1.6E-03	-3.9E-02	1.02	998.3	0.96	1.1E-07	1.1E-07
4	0.0	2.7E-03	-3.8E-02	1.02	998.3	0.44	4.6E-08	1.0E-07
5	0.0	3.3E-03	-3.7E-02	1.02	998.3	-0.06	9.4E-09	-1.5E-07
6	0.0	3.2E-03	-3.7E-02	1.02	998.3	0.64	6.0E-08	9.3E-08
7	0.0	1.7E-03	-3.9E-02	1.02	998.3	1.97	3.5E-07	1.8E-07
8	0.0	2.3E-03	-3.8E-02	1.02	998.3	1.46	2.2E-07	1.5E-07
9	0.0	3.0E-03	-3.8E-02	1.02	998.3	0.95	1.1E-07	1.2E-07
10	0.0	3.3E-03	-3.7E-02	1.02	998.3	0.65	7.4E-08	1.1E-07
11	0.0	3.5E-03	-3.7E-02	1.02	998.3	0.43	5.0E-08	1.2E-07
12	0.0	4.1E-03	-3.7E-02	1.02	998.3	-0.06	8.7E-09	-1.4E-07
13	1.0	4.9E-02	8.3E-03	1.02	998.3	1.98	2.4E-08	1.2E-08
14	1.0	4.9E-02	8.8E-03	1.02	998.3	1.47	1.3E-08	8.8E-09
15	1.0	5.0E-02	9.1E-03	1.02	998.3	0.95	6.8E-09	7.2E-09
16	1.0	4.7E-02	6.6E-03	1.02	998.3	0.45	2.6E-09	5.9E-09
17	2.0	5.8E-02	1.7E-02	1.02	998.3	3.00	1.5E-08	5.2E-09
18	2.0	5.8E-02	1.7E-02	1.02	998.3	2.49	1.1E-08	4.6E-09
19	2.0	5.8E-02	1.8E-02	1.02	998.3	1.97	7.2E-09	3.6E-09
20	4.0	7.1E-02	3.1E-02	1.02	998.3	3.00	6.5E-09	2.2E-09
21	4.0	7.2E-02	3.1E-02	1.02	998.3	4.02	1.3E-08	3.1E-09
22	4.0	7.2E-02	3.1E-02	1.02	998.3	3.51	9.9E-09	2.8E-09
23	8.0	8.9E-02	4.8E-02	1.02	998.3	4.02	4.9E-09	1.2E-09
24	8.0	8.9E-02	4.8E-02	1.02	998.3	3.51	3.9E-09	1.1E-09
25	8.0	8.9E-02	4.9E-02	1.02	998.3	2.99	2.4E-09	8.0E-10
26	4.0	8.1E-02	4.0E-02	1.01	998.3	3.51	4.9E-09	1.4E-09
27	2.0	7.3E-02	3.3E-02	1.01	998.3	3.51	6.5E-09	1.9E-09
28	1.0	6.7E-02	2.6E-02	1.01	998.3	3.51	1.2E-08	3.4E-09
29	0.0	1.2E-02	-2.9E-02	1.01	998.3	3.50	4.4E-07	1.3E-07
30	0.1	2.5E-02	-1.6E-02	1.01	998.2	4.27	1.8E-07	4.1E-08
31	0.1	2.5E-02	-1.6E-02	1.01	998.2	3.75	1.5E-07	4.1E-08
32	1.0	4.9E-02	8.6E-03	1.01	998.2	4.27	2.9E-08	6.8E-09
33	1.0	4.9E-02	8.7E-03	1.01	998.2	3.75	2.5E-08	6.7E-09
34	2.0	5.9E-02	1.8E-02	1.01	998.2	4.26	1.4E-08	3.4E-09
35	2.0	5.9E-02	1.8E-02	1.01	998.2	3.76	1.2E-08	3.1E-09
36	4.0	7.0E-02	3.0E-02	1.01	998.2	4.50	6.2E-09	1.4E-09
37	4.0	7.1E-02	3.0E-02	1.01	998.2	4.26	6.8E-09	1.6E-09
38	8.0	8.6E-02	4.6E-02	1.01	998.2	4.51	1.9E-09	4.2E-10
39	4.0	7.7E-02	3.6E-02	1.01	998.2	4.51	2.1E-09	4.7E-10

	σ	LVDT_Ave.	Displacement	Viscosity	Density	Δh	Q	T
	(MPa)	(mm)	(mm)	(mPa-s)	(kg/m^3)	(m)	(m^3/s)	(m^2/s)
40	2.0	6.9E-02	2.8E-02	1.01	998.2	4.50	4.9E-09	1.1E-09
41	1.0	6.2E-02	2.1E-02	1.01	998.2	4.50	5.9E-09	1.3E-09
42	0.1	4.1E-02	4.8E-04	1.01	998.2	4.26	3.6E-08	8.5E-09
43	1.0	5.8E-02	1.7E-02	1.01	998.2	4.27	8.2E-09	1.9E-09
44	1.0	5.8E-02	1.7E-02	1.01	998.2	4.50	7.8E-09	1.7E-09
45	2.0	6.5E-02	2.5E-02	1.01	998.2	4.51	3.6E-09	8.0E-10
46	4.0	7.4E-02	3.4E-02	1.01	998.2	4.51	2.9E-09	6.5E-10
47	8.0	8.9E-02	4.8E-02	1.01	998.2	4.50	1.1E-09	2.4E-10
48	4.0	7.8E-02	3.7E-02	1.01	998.2	4.51	1.3E-09	2.8E-10
49	2.0	7.0E-02	2.9E-02	1.01	998.2	4.50	3.3E-09	7.3E-10
50	1.0	6.1E-02	2.0E-02	1.01	998.3	4.50	3.9E-09	8.7E-10
51	1.0	6.1E-02	2.0E-02	1.01	998.3	4.50	3.1E-09	6.9E-10
52	0.1	4.1E-02	0.0	1.01	998.3	4.51	3.1E-08	6.9E-09
53	1.0	5.4E-02	1.3E-02	0.98	998.4	4.27	8.8E-09	2.1E-09
54	2.0	6.2E-02	2.2E-02	0.98	998.3	4.27	5.1E-09	1.2E-09
55	2.0	6.3E-02	2.2E-02	0.98	998.2	4.50	4.3E-09	9.5E-10
56	10.0	9.3E-02	5.2E-02	0.98	998.1	5.29	1.9E-09	3.5E-10
57	20.0	1.2E-01	8.0E-02	0.98	998.1	5.29	1.4E-09	2.6E-10
58	20.0	1.2E-01	8.0E-02	0.99	998.2	5.29	4.4E-10	8.3E-11
59	30.0	1.4E-01	1.0E-01	0.98	998	5.29	3.2E-10	6.0E-11
60	37.5	1.6E-01	1.2E-01	0.98	998.1	5.30	1.9E-10	3.6E-11

2.3.4 Mechanical properties

As part of the POST study, intact rock mass properties have been determined on core samples extracted from block 15.2.2.1 (Figure 2-17 and Table 2-5). The intact rock properties of block 19.6.1.4 used in Task 10.2.2 are assumed to be nearly identical. For ten samples, the uniaxial compressive strength, Young's modulus and Poisson's ratio have been determined. The indirect tensile strength has been measured on thirty additional samples. The mechanical parameters of the fracture surface were referenced from Schmidt hammer tests conducted on sampled specimens, 2N2-CNL, 3N3-CNL, and 4N4-CNL near Block 15.2.2.1 (Table 2-6).

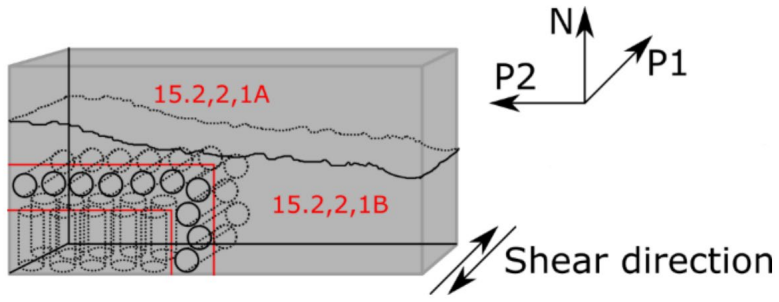

Figure 2-17. *Schematic diagram of the sampled intact rock.*

Table 2-5. Mechanical parameters obtained from the sampled intact rock

Direction (or position)	Specimen ID	Diameter [mm]	Height [mm]	Uniaxial compressive strength [MPa]	Young's modulus [GPa]	Poisson's ratio [-]
Parallel shear direction (P1)	D54P2	54.2	135.7	269.4	72.9	0.321
	D54P3	54.2	134.9	269.9	74.0	0.326
	D54P4	54.2	134.9	273.7	72.1	0.308
	D54P5	54.2	134.9	266.2	73.0	0.317
	D54P8	54.2	134.9	276.5	73.4	0.313
	Average (standard deviation)	-	-	271.1 (4.0)	73.1 (0.7)	0.32 (0.01)
Normal to shear direction (N)	D54N3	54.2	135.3	269.8	74.6	0.324
	D54N4	54.2	135.5	264.1	71.7	0.303
	D54N7	54.2	135.8	268.4	73.0	0.307
	D54N8	54.2	135.8	267.8	73.0	0.314
	D54N10	54.2	135.7	269.4	72.4	0.313
	Average (standard deviation)	-	-	267.9 (2.3)	72.9 (1.1)	0.31 (0.01)

Table 2-6. Table of Schmidt hammer rebound parameters, using the 2N2-CNL lower surface test as an example

	Downward +90° ↓				
	θ = 90				
Rebound	R_L - Lower	x2(θ)	(V2(θ))^2	(V2)^2	R_L - corrected
1	45	0.03285	2.76170	2.42896	48
2	31	0.02263	1.44875	1.27420	35
3	46	0.03358	2.87117	2.52523	49
4	36	0.02628	1.87061	1.64523	40
5	50	0.03650	3.32994	2.92873	53
6	25	0.01825	1.01152	0.88964	29
7	29	0.02117	1.29464	1.13866	33
8	33	0.02409	1.61122	1.41709	37
9	52	0.03796	3.57187	3.14151	55
10	52	0.03796	3.57187	3.14151	55
11	46	0.03358	2.87117	2.52523	49
12	44	0.03212	2.65433	2.33452	47
13	36	0.02628	1.87061	1.64523	40
14	27	0.01971	1.14890	1.01047	31
15	46	0.03358	2.87117	2.52523	49
16	33	0.02409	1.61122	1.41709	37
17	36	0.02628	1.87061	1.64523	40
18	22	0.01606	0.82113	0.72220	26
19	52	0.03796	3.57187	3.14151	55
20	30	0.02190	1.37065	1.20551	34

2.4 Pragmatic validation

Two key aspects of pragmatic validation are the *a priori* determination of the model purpose and the *a posteriori* determination of the model's domain of applicability. Per the description of Task 10, the intended purpose should be beyond the immediate model use of matching or reproducing experimental data, i.e., the intended use typically implies an extrapolation in time or space, or an extrapolation in applied boundary or initial conditions. The predictive power of the extrapolation is assessed by prediction-outcome exercises.

In the case of Task 10.2.2, the extrapolation is achieved by predicting flows for conditions of higher normal loads. This extrapolation constitutes the prediction-outcome exercise of Task 10.2.2. In addition to the prediction-outcome exercise, additional items should be addressed as part of the pragmatic validation. At Task Force Meeting 40, May 10-12, 2022, in Kalmar (TF #40), the following main items were presented to be considered part of a Pragmatic Validation Workflow.

1. Definition of the model purpose: Specify the intended purpose of the model, which is a crucial aspect of model evaluation, as the model purpose helps determine the benchmark and standards for critical evaluation.
2. Domain of model applicability and prediction, including limits of applicability identified in the Pragmatic Validation exercise and limitations required to make the exercise possible.
3. Determination of critical aspects: Identify aspects of modelling that are specific to the intended use and which therefore require validation.
4. Definition of performance measures and criteria: Discussion of the basis for performance measures and acceptance criteria specific to the model purpose and conceptual/numerical models used.
5. Conceptual assumptions being tested by the Pragmatic Validation exercise (e.g., DFN geometric models, parallel plate flow, correlations between geometric/hydraulic/geomechanical properties).
6. Approaches for derivation of numerical parameters being tested by the Pragmatic Validation exercise (e.g., boundary conditions, material properties, fracture geometries, microstructural models).
7. Understanding of the scope and limitations of experimental data and theoretical concepts being used to support modelling and performance measures. The accuracy of both the model output and data must be sufficiently high that they are discriminative in the evaluation of the acceptance criteria.
8. Sensitivity and uncertainty analysis of influential factors: Provide details of the sensitivity and uncertainty analyses necessary to support a determination of which factors are most critical to Pragmatic Validation.
9. Prediction-outcome exercises: Details of modelling carried out to support prediction-outcome exercises, including identification of uncertainties in predictions due to underlying data, and uncertainties due to underlying assumptions and simplifications.
10. Model evaluation, documentation, and model audit: Qualitative and quantitative assessment of model performance measures as compared to the prediction-outcome exercise models.
11. Pragmatic validation statements: Explicitly state what level of pragmatic validation was achieved by the exercise as conducted, how this exercise could be improved, and what might be required to achieve validation sufficient for the model purpose.

3 Modelling and methodology

3.1 Modelling tasks

Based on the methodology developed for geometric evaluation in Task 10.2.1 using the four 100 x 70 mm^2 fractures, the NTU modelling team evaluates the 200 x 200 mm^2 fracture's geometric characteristics and predicts water flow through this fracture under various normal loadings.

3.1.1 Model purpose

The purpose of the NTU modelling team is to conduct high-resolution fracture surface characterization and develop detailed flow simulation analyses within the transmissivity field of the single fracture. The in-house developed software is designed to deal with scanned fracture surfaces, evaluate the aperture fields, derive transmissivity fields, and predict water flow through the fracture under various normal loading conditions with associated uncertainties.

In this modelling framework, mechanical-hydraulic coupling experiments provide main measurements of applied normal loads, resulting displacements, hydraulic boundary conditions, and flow rates. The stress–displacement data are used to calibrate the deformation behaviour of fracture surfaces, enabling the estimation of aperture fields. These aperture fields are then used to calculate transmissivity fields, which can be used to simulate water flow. The predicted results of flow simulations are validated against experimental flow measurements.

3.1.2 Model description

In accordance with the model purpose, the modelling framework is divided into three components:

1. Geometric alignment and fracture surface characterization

The first step involves aligning the upper and lower fracture surfaces. The Iterative Closest Point (ICP) algorithm is applied for rigid-body registration, with additional vertical translation along the z-axis introduced when necessary to reflect physically possible contact configurations. This adjustment is typically calibrated the mechanical parameters to match experimental measurements. Following alignment, geometric parameters are evaluated to quantify the topography of surfaces.

2. Mechanical contact modelling

The second component simulates the deformation behaviour of the upper and lower surfaces under normal loading. A contact model is developed to evaluate how the aligned fracture surfaces deform with application of varying loads, resulting in aperture fields. The resolution of discretization is selected to meet the requirements that the results of hydraulic modelling could show channelling effects while preserving key geometric features.

3. Hydraulic modelling

In the final component, each aperture field is converted into a transmissivity field using cubic law. Based on a transmissivity field, a finite volume method is employed to solve the steady-state form of the Laplace equation $T\nabla^2 h = 0$, where h is the hydraulic head and T represents the transmissivity. The solution yields the hydraulic head field. The hydraulic head field is used to calculate Darcy velocity field, flow rate field, and total discharge across the outflow boundary. These outcomes provide the basis for analysing flow behaviour through the fracture, including total flow rate predictions and channelling effects.

3.1.3 Determination of critical aspects

1. It is assumed that the fracture surfaces are optimally matched during the HM experiments. Therefore, a point-cloud alignment algorithm was employed to achieve the most probable fracture matching condition.
2. The mechanical model considers only the fracture closure resulting from deformation in the contact regions. Both upper surface and lower surface are discretized into rectangular elements. Subtracting the elevation of the bottom surface from that of the top surface yields an aperture field.
3. In the conceptual hydraulic model, governing equation is developed according to Darcy's law and mass conservation based on the transmissivity field which is discretized as rectangular elements.
4. The hydraulic parameter required in the governing equation in the hydraulic model is transmissivity. The estimation of transmissivity is based on the cubic law.
5. The flow simulation results yield the steady-state hydraulic head field of the fracture. Subsequently, the Darcy velocity and flow rate are calculated using the hydraulic gradient, average transmissivity between adjacent elements, and size of each element.
6. The flow rate at the outflow boundary is the sum of the flow rates across all elements located on the outflow boundary. The flow rate of every element is calculated based on the Darcy velocity in the direction perpendicular to the outflow boundary as well as the cross-section area in the direction parallel to the outflow boundary.

3.1.4 Model parameters

The scanned upper and lower fracture wall surfaces serve as the raw data for our modelling exercise. Based on the topography of the upper and lower fracture wall surfaces, associated quantitative evaluation of the roughness of the two surfaces is conducted. This includes calculating the joint roughness coefficient (JRC; Barton and Choubey, 1977), Root-mean-square (RMS) of profile slope, Z_2 (Yu and Vayssade, 1991) and Directional roughness metric, $2A_0\,\theta^*_{max}/(C+1)$ (Tatone and Grasselli, 2009).

After the upper and lower fracture surfaces are aligned, the aperture field $\boldsymbol{E(x,y)}$ is computed by discretizing both surfaces onto the same grid and subtracting the elevation of the lower surface $\boldsymbol{Z_l(x,y)}$ from that of the upper surface $\boldsymbol{Z_u}$ $\boldsymbol{(x,y)}$.

$$\boldsymbol{E}\,(\boldsymbol{x},\boldsymbol{y}) = \boldsymbol{Z_u}(\boldsymbol{x},\boldsymbol{y}) - \boldsymbol{Z_l}(\boldsymbol{x},\boldsymbol{y}) \tag{3-1}$$

The aperture field not only indicates the space available for water flow but also indicates zones where the aperture approaches zero, i.e., zones where the upper and lower fracture wall surfaces are in contact. These contact zones are the primary locations where deformation occurs due to normal loading. Under applied normal loading, deformation occurs primarily in the rock mass surrounding the asperity contacts between the upper and lower fracture surfaces. These localized compressive deformations cause the overall fracture surfaces to move closer together, not only maintaining contact at asperities but also reducing the aperture in nearby non-contact regions. As the loading increases, additional asperities may come into contact, further altering the contact pattern and contributing to the progressive fracture closure. To consider the impact of normal loading on the aperture field, the mechanical properties of the contact zones must be taken into consideration. Therefore, we will refer to the properties of intact rock mentioned in Section 2.3.4.

3.1.5 Identification of influential factors

The provided upper and lower fracture surfaces are regarded as perfect, i.e., the data exactly describe the geometric characteristics of the surfaces of both sides of the fracture. How the upper and lower fracture wall surfaces are assembled may affect the contact zones between them, further influencing the aperture fields under different normal loadings.

The point clouds of the two surfaces are initially in their measured, potentially misaligned positions. A rigid-body transformation is therefore applied to achieve the best geometric match between the two surfaces, typically using an ICP algorithm. The alignment criterion in ICP is to minimize the root-mean-square (RMS) distance between matched points on the two surfaces. However, this objective function may lead to excessive vertical proximity between the surfaces, resulting in unrealistically small apertures or even interpenetration. To mitigate this, a subsequent vertical translation along the z-axis direction is applied to ensure a physically reasonable initial separation. The magnitude of this z-axis direction translation becomes an influential factor in determining the initial the contact state and the aperture field. The magnitude of the translation is calibrated jointly with influential factors in the mechanical model to reflect the reasonable deformation behaviour. After applying this adjustment, regions where interpenetration still occurs are interpreted as contact zones.

In the mechanical model, the deformation behaviour of the fracture under normal loading is primarily governed by the elastic properties of the contact zones. Among the elastic parameters, the Young's modulus plays a particularly influential role. Although its value is typically obtained from laboratory tests on intact rock cores, the Young's modulus of fracture contact regions is likely to be higher or lower due to surface irregularities, microcracks, and localized yielding. As the mechanical deformation in the simulation focuses on asperity-scale interactions, the Young's modulus is treated as a key influential factor in calibrating the normal deformation behaviour of the model.

3.1.6 Uncertainty analyses

The primary source of uncertainty in this modelling approach arises from different alignment scenarios of the fracture surfaces, resulting in different mechanical deformation behaviours. One key uncertainty lies in the definition of the initial contact state between the upper and lower fracture surfaces. Although the point clouds were aligned using the ICP algorithm, a range of physically possible initial contact scenarios was considered by vertically translating one of the surfaces prior to mechanical simulation. This z-axis direction translation allows for an investigation of how different contact states influence the evolution of contact zones, aperture fields, and transmissivity fields.

Although the mechanical model discretizes the fracture surfaces into elements that capture asperity-scale variations, the spatial resolution may be insufficient to fully resolve micro-scale roughness and local heterogeneity in contact strength. As a result, while the model can simulate fully closed contact zones, such complete closure is rarely to occur in reality due to micro-scale surface irregularities and spatially varying mechanical properties. In the hydraulic model, these fully closed elements are assigned a minimum transmissivity value to reflect potential residual flow through micro-pathways that may exist in real fractures.

3.1.7 Workflow describing the modelling process

The overall modelling workflow adopted in this study is summarized in Figure 3-1 It is structured into three modules: the Geo-Module, the Mech-Module, and the Hydro-Module.

(1) Geo-Module

- **Alignment of fracture surfaces**

The ICP algorithm is applied to determine the best matching of these two surfaces. The input are two-point clouds and an initial transformation that roughly aligns the source point cloud to the target point cloud. The output is a refined transformation that tightly aligns the two-point clouds. The ICP algorithm is frequently used for matching three-dimensional shapes, such as free-form curves and surfaces (Besl and McKay, 1992).

The point cloud describing the lower surface is selected as the reference cloud, and the upper surface is selected as cloud to be aligned. These two surfaces are assumed to exhibit similar undulating features, such as peak-valley patterns and contour lines. Based on this assumption, the ICP algorithm implemented in CloudCompare is applied to align the upper surface to the lower surface.

The alignment process is considered complete once the root mean square (RMS) error converges below 1×10^{-5} mm, which is set as the convergence criterion in this study. This threshold ensures that the alignment reflects a high degree of geometric consistency.

$$RMS = \left(\frac{1}{N}\sum_{i=1}^{N}|p_i - q_i|\right)^{1/2} \quad (3\text{-}2)$$

where p_i and q_i are the matched point pairs from the reference and aligned clouds respectively, and N is the total number of point pairs.

- **Roughness indices evaluation**

Quantitative evaluation of the roughness of a fracture in terms of joint roughness coefficient (JRC; Barton and Choubey, 1977), Root-mean-square (RMS) of profile slope, Z_2 (Yu and Vayssade, 1991) and Directional roughness metric, $\theta^*_{max}/(C+1)$ (Tatone and Grasselli, 2009) are assessed, with reference to the assigned local Cartesian coordinate. The JRC is estimated using visual inspection with the reference of the so-called standard profile suggested by Barton and Choubey (1977). The RMS of profile slope, Z_2, is typically calculated using a distance dx of 0.05 mm. And the directional roughness metric, $\theta^*_{max}/(C+1)$ are also evaluated. We follow the suggestion of Tatone and Grasselli (2009) regarding the coefficient A_0 (normalized area of the surface corresponding to an angular threshold of 0° in the chosen analysis direction) and determine $2A_0\,\theta^*_{max}/(C+1)$ using a polar plot for visualization.

- **Discretization and Contact definition**

Once the discretization resolution is determined, the elevation difference between the upper and lower surfaces is calculated using Equation 3-1 and is regarded as the aperture field. A contact zone is defined as any zone where the elevation of the upper surface minus the elevation of the lower surface is less than or equal to zero.

- **Adjustment of Initial contact state**

The adjustment of the contact state here refers to applying a translation along the z-axis direction after the ICP algorithm to obtain a possible initial contact state. Whether this initial contact state is suitable or not depends on whether the stress-displacement curve aligns with the experimental data, after being imported into the Mech-Module.

(2) Mech-Module

- **Mechanical model and Aperture field under normal stress**

In the Mech-Module, the relationship between normal loads and deformation of the fracture specimen is simplified using basic principles of Mechanics of Materials. Specifically, the incremental axial displacement $\Delta\delta_z$ caused by incremental stress $\Delta\sigma$ of the contact columns is estimated based on the assumption of elastic deformation, and is governed by the Young's modulus E and the column height L (Equation 3-3).

In addition, the lateral confinement effect is considered through the Poisson's ratio v, which relates axial compression to lateral expansion of the material. Although the full three-dimensional stress-strain behavior is not explicitly modeled, these parameters control how individual contact asperities deform under increasing loads.

The average normal incremental stress $\Delta\sigma$ in the contact regions is then used to evaluate the fracture closure behavior, assuming a distributed contact load and isotropic material response within each column.

$$\Delta\delta_z = \frac{\Delta\sigma}{E} \times \left(1 - \frac{2v^2}{1-v}\right) \times L \tag{3-3}$$

Based on Equation 3-3, this simplified contact model provides an approach for estimating aperture fields under different normal loadings (Figure 3-2).

(3) Hydro-Module

- **Estimation of transmissivity components**

In this study, transmissivity field $T(x, y)$ is estimated from the aperture field $E(x, y)$ using the cubic law (Equation 3-4), which assumes laminar flow between two parallel plates. The transmissivity at each location is calculated as:

$$T(x, y) = \frac{gE(x,y)^3}{12v} \ (m^2/s) \tag{3-4}$$

where v is the kinematic viscosity of the fluid (m^2/s), and g is gravity acceleration. This formulation provides a spatially distributed transmissivity field that reflects the heterogeneity of the aperture field, and serves as input for the subsequent flow simulations.

- **Flow modelling and demonstration**

The Laplacians equation that describes steady-state flow through the fracture, $\boldsymbol{T}\nabla^2 h = 0$, is solved using the finite volume method to follow mass conversion, resulting in a linear system of equations of the form, $[A][h] = [b]$, (Figure 3-3) where:

- $[A]$ is a sparse coefficient matrix representing the transmissivity-weighted connectivity between adjacent nodes.
- $[h]$ is the unknown vector of hydraulic heads at all nodes.
- $[b]$ is the boundary condition vector containing constant head values or zero-flux terms.

For example, the following equation is for node h_j^i:

$$T_{left}\frac{(h_{j-1}^i - h_j^i)}{L_x}L_y + T_{right}\frac{(h_{j+1}^i - h_j^i)}{L_x}L_y + T_{back}\frac{\left(h_j^{i-1} - h_j^i\right)}{L_y}L_x + T_{for}\frac{\left(h_j^{i+1} - h_j^i\right)}{L_y}L_x = 0$$

Where L_x and L_y are the size in x-axis direction and y-axis direction of element respectively. T_{left}, T_{right}, T_{back}, T_{for} are the average transmissivity between h_{j-1}^i and h_j^i, h_{j+1}^i and h_j^i, h_j^{i-1} and h_j^i, h_j^{i+1} and h_j^i, respectively.

Two directions of water flow are considered, i.e., from Face 1 to Face 3 along the x-direction, and from Face 2 to Face 4 along the y-direction. During the x-directional flow modelling, the higher heads are assigned to the Face 1 with two impermeable boundaries (Face 2 and Face 4) and lower heads on Face 3. The solved $[h]$ represents the head fields after steady state is reached. Similarly, the flow along the y-direction can be modelled.

After the steady-state head field is obtained, the head difference between two neighbouring positions is used to calculate the Darcy velocity field and the flow rate field.

To quantify the concentration of flow within fractures, we adopted the channelling factor proposed by Maillot et al. (2016), expressed as follows:

$$d_{qnet} = \frac{1}{\sum S_m} \times \frac{(\sum S_m \times Q_m)^2}{(\sum S_m \times {Q_m}^2)} \qquad (3\text{-}5)$$

Where S_m is the area of each computing element and Q_m is the corresponding flow rate of each element.

3.1.8 Pragmatic validation aspects

The aperture field under different loading stages was obtained by calibrating the mechanical model using LVDT-recorded displacements. The transmissivity field was then derived directly from the calibrated aperture field using the theoretical cubic law. The simulated discharge through the fracture under varying normal loads (0 MPa to 40 MPa) was subsequently compared with experimental flow rate data to assess the predictive performance of the model.

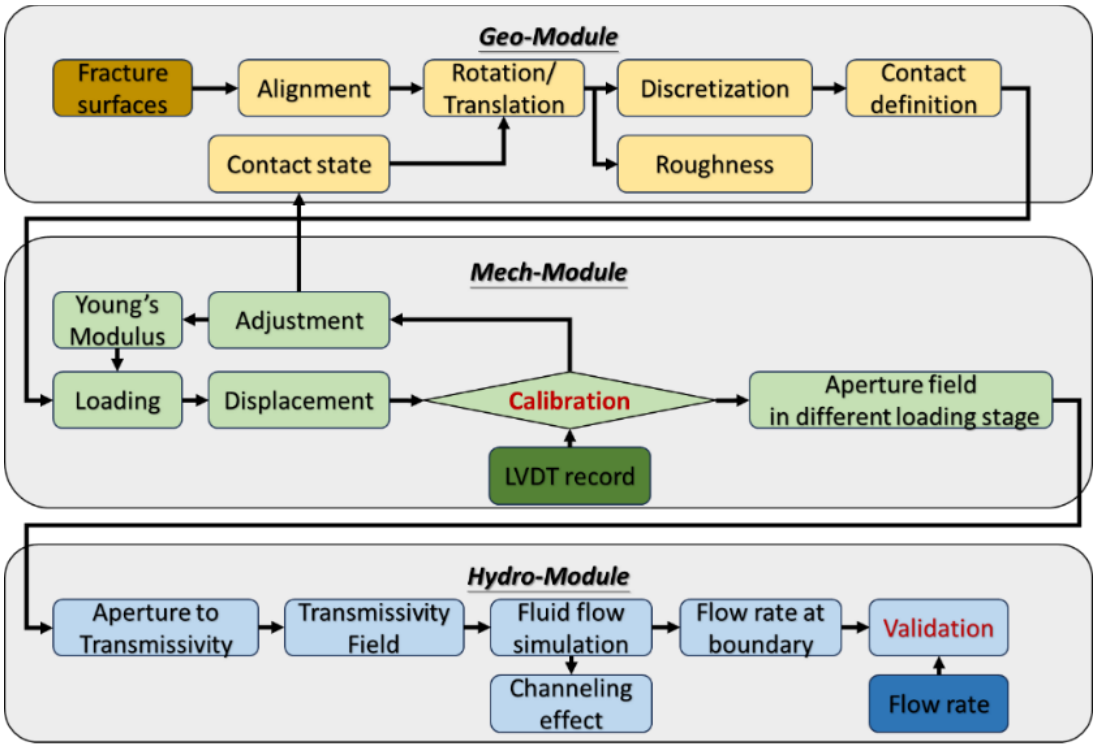

Figure 3-1. *NTU Modelling flowchart.*

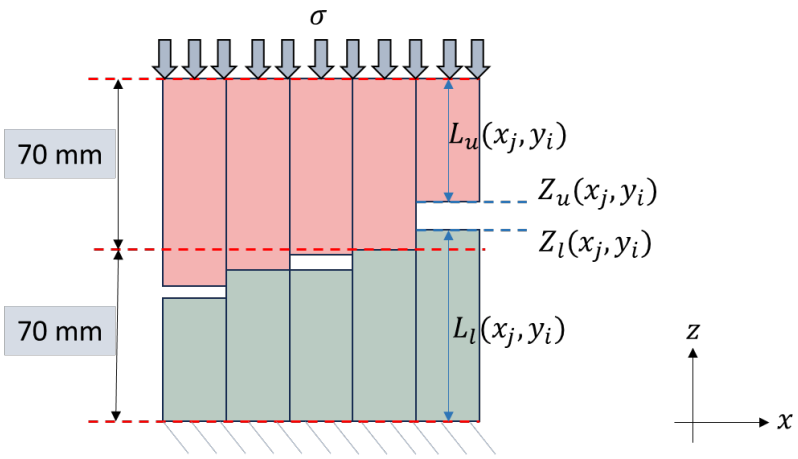

Figure 3-2. *A 2D schematic diagram of the mechanical model. The 70 mm setting is based on the LVDT gauge length shown in Figure 2-9.*

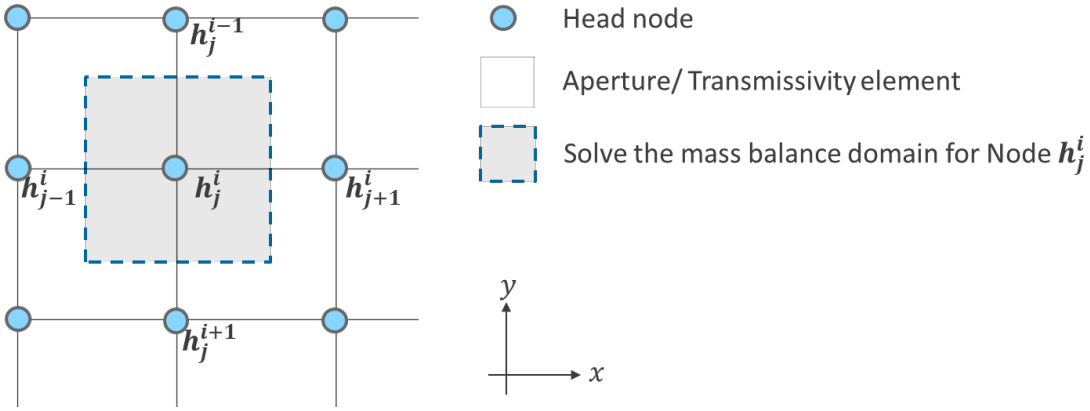

Figure 3-3. *Schematic diagram of the FVM used in the hydraulic model.*

3.2 Prediction and validation of flow along a fracture at different normal loads

This section aims to evaluate the hydro-mechanical behaviour of a single fracture subjected to increasing normal loads. A key objective is to assess whether a model calibrated using mechanical displacement measurements can accurately predict the reduction in fracture transmissivity and flow rate as loading increases.

3.2.1 Definition of the performance measures and criteria

To evaluate the model performance, the following measures were selected:

- Flow rate (Q): The total discharge through the fracture domain under different combinations of normal load and hydraulic gradient. This is the primary quantity used for comparison against experimental measurements.
- Channelling factor (d_{qnet}): The degree of flow localization within the fracture plane, intended to assess the spatial heterogeneity in transmissivity and velocity fields. Although a formal analysis was not performed, the simulated velocity fields were visually inspected to identify flow localization behaviour under loading.

The model is considered successful if it correctly predicts the decreasing trend of flow rate with increasing normal stress, and the simulated values fall within an acceptable range of the experimental data.

3.2.2 Task 10.2.2c: Prediction-outcome exercise of flow along an unopened fracture at different normal loads

After obtaining a possible initial contact state of fracture surfaces, the mechanical model is used to estimate the closure behaviour of the fracture specimen under applied normal loads. The model was calibrated using LVDT displacement data, resulting in predicted aperture fields under each load.

Using the cubic law, transmissivity fields were derived from the aperture fields, and steady-state flow simulations were conducted using a finite volume solver. Boundary conditions were assigned with different simulations conducted for flow directions from Face 1 to Face 3 and from Face 2 to Face 4.

The predicted flow rates were compared to experimental measurements under equivalent loading and flow conditions. The flow simulations reproduced the general trend of decreasing discharge with increasing load, and captured the emergence of channelized flow paths.

This modelling effort demonstrates the predictive capability of the coupled hydro-mechanical model under extrapolated mechanical conditions, and supports the goals of pragmatic validation.

4 Results

Geometrical characteristics, modelled water head and flow rate fields, and the influence of normal loading on water flow through the 200 x 200 mm^2 fracture are introduced in the following subsections.

4.1 Geometrical characteristics

4.1.1 Roughness indices for entire fracture

Directional roughness metrics, $\theta^*_{max}/(C+1)$ (Tatone and Grasselli, 2009) of the scanned lower surface of the 200 x 200 mm^2 fracture are evaluated. We follow the suggestion of Tatone and Grasselli (2009) to involving the A_0, normalized area of the surface corresponding to an angular threshold of 0° in the chosen analysis direction. Figure 4-1 shows the polar plots of $2A_0\,\theta^*_{max}/(C+1)$ for the 200 x 200 mm^2 fracture. Table 4-1 lists the calculated results of $2A_0\,\theta^*_{max}/(C+1)$ for the fracture.

Figure 4-2 shows the 2D profiles along the *x*- and *y*-axis of the scanned lower surface of the 200 x 200 mm^2 fracture. Using visual inspection with the reference of the so-called standard profile suggested by Barton and Choubey (1977), the JRCs of these *y*-axis-parallel profiles are estimated to be 3.5-9.9 with an average of 6.7 and standard deviations of 1.6, and *x*-axis-parallel profiles of 4.0-9.4 with an average of 5.7 and standard deviations of 1.7. The JRC in the *x*-axis-parallel directions represent the surface characteristics along the flow paths from Face 1 to Face 3. Similarly, The JRC in the *y*-axis-parallel directions represent the surface characteristics along the flow paths from Face 2 to Face 4. Table 4-2 lists the results of the JRC estimation of the 200 x 200 mm^2 fractures.

The RMS of profile slope, Z_2 (Yu and Vayssade, 1991), is also calculated using a distance *dx* of 1 mm. The Z_2 values of the upper and lower surfaces of the 200 x 200 mm² fracture have an average of 0.33 in the *x*-axis direction and 0.30 in the *y*-axis direction, respectively. Table 4-3 lists the Z_2 values of the 200 x 200 mm^2 fracture.

Among the above three parameters, we believe that Z_2 is more related to the ease of flow along the flow path although it may not fully represent the exact geometry of the flow path. It can also be observed that even though the average values of Z_2 in the two directions are similar, the COV (Coefficient of Variation) differs significantly. Therefore, we intend to use Z_2 as the geometric parameter in the transmissivity conversion formula.

(a) Lower surface (b) Upper surface (c) Directional Roughness

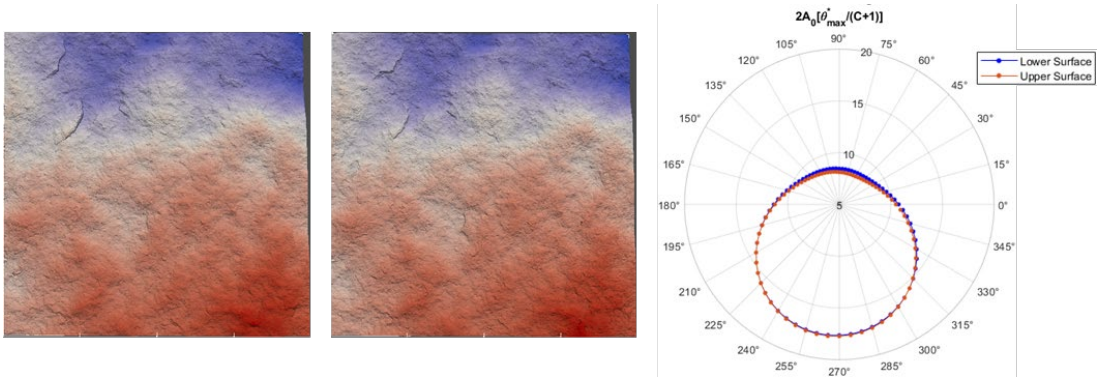

Figure 4-1. *Polar plots of calculated* $2A_0\theta^*_{max}/(C+1)$ *for 200x200 mm^2 fracture.*

Table 4-1. Summary of calculated $2A_0\theta^*_{max}/(C+1)$ for 200x200 mm^2 fracture.

Surface	$2A_0[\theta^*_{max}/(C+1)]$			Anisotropy
	Max.	min.	Ave.	
Upper	17.75	8.09	11.95	2.19
Lower	17.67	8.44	12.10	2.09

(a) *y*-axis parallel profiles (b) *x*-axis parallel profiles

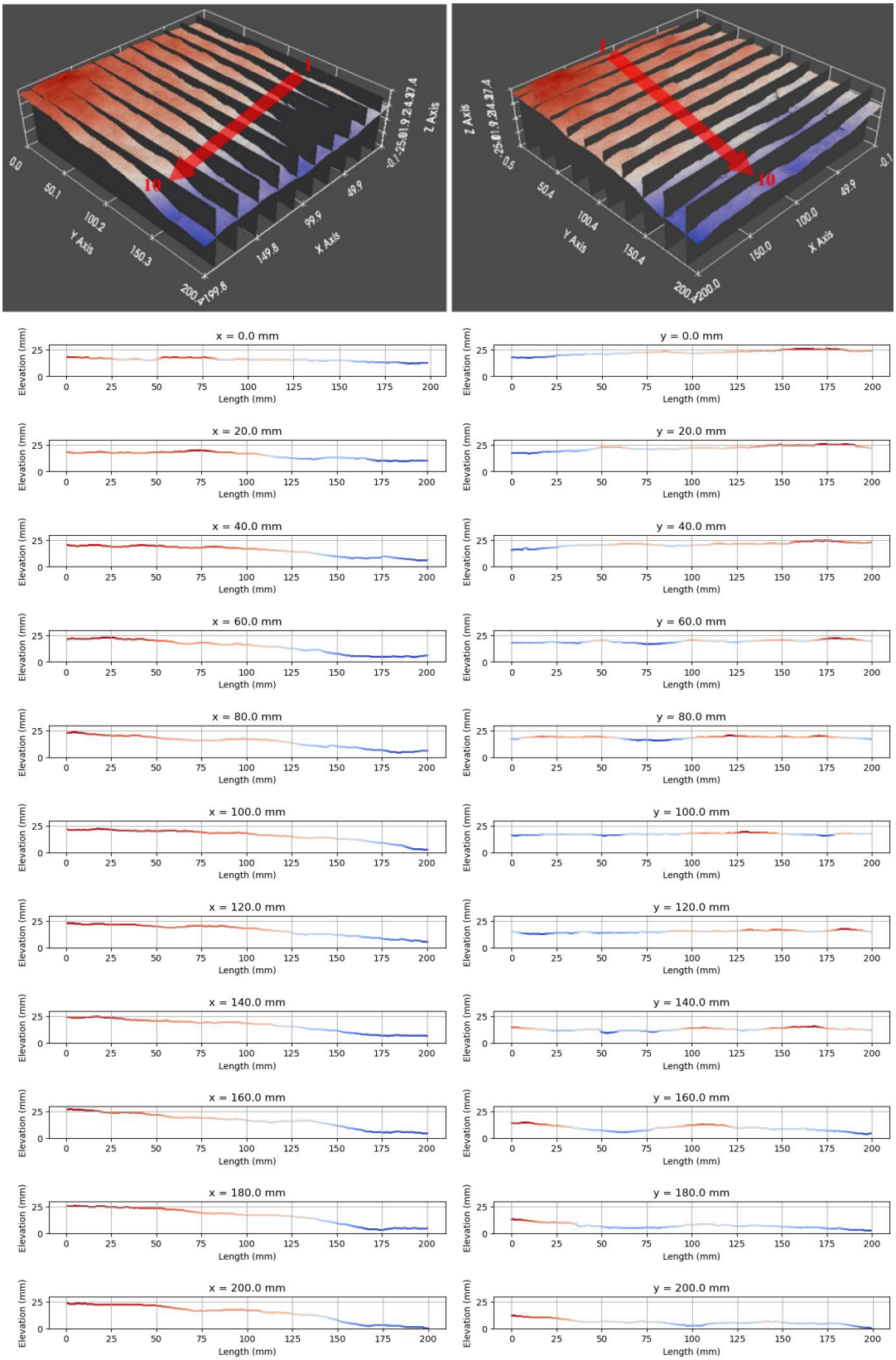

Figure 4-2. *2D profiles along (a) y- and (b) y-axis of scanned lower surface of 200x200 mm^2 fracture.*

Table 4-2. Summary of JRC estimation for 200 x 200 mm² fracture

(a) *y*-axis-parallel profiles

Surface	*y*-axis-parallel profiles (Face 2-Face 4)										
	x=0 mm	x=20 mm	x=40 mm	x=60 mm	x=80 mm	x=100 mm	x=120 mm	x=140 mm	x=160 mm	x=180 mm	x=200 mm
Upper	3.6	6.9	5.6	6.9	6.1	9.9	6.2	5.3	8.0	7.7	7.4
Lower	3.5	6.9	6.0	6.8	6.2	9.9	6.2	5.3	8.0	7.6	7.4

(b) *x*-axis-parallel profiles

Surface	*x*-axis-parallel profiles (Face 1-Face 3)										
	y=0 mm	y=20 mm	y=40 mm	y=60 mm	y=80 mm	y=100 mm	y=120 mm	y=140 mm	y=160 mm	y=180 mm	y=200 mm
Upper	5.0	6.7	4.4	4.3	5.3	4.0	4.0	5.8	9.4	6.8	7.3
Lower	5.0	6.7	4.4	4.3	5.3	4.0	4.0	5.8	9.4	6.8	7.3

(c) Maximum, minimum, mean value and standard deviation of JRC

Surface	y-axis parallel profiles (Face 2-Face 4)					*x*-axis parallel profiles (Face 1-Face 3)				
	Max.	Min.	Mean	Stdev	COV(%)	Max.	Min.	Mean	Stdev	COV(%)
Upper	9.9	3.7	6.7	1.6	24	9.4	4.0	5.7	1.7	30
Lower	9.9	3.5	6.7	1.6	24	9.4	4.0	5.7	1.7	30

Table 4-3. Summary of calculated Z_2 for 200 x 200 mm² fracture.

(a) *y*-axis-parallel profiles

Surface	*y*-axis-parallel profiles (Face 2-Face 4)										
	x=0 mm	x=20 mm	x=40 mm	x=60 mm	x=80 mm	x=100 mm	x=120 mm	x=140 mm	x=160 mm	x=180 mm	x=200 mm
Upper	0.28	0.25	0.29	0.30	0.30	0.28	0.28	0.27	0.30	0.31	0.35
Lower	0.30	0.25	0.49	0.29	0.33	0.26	0.27	0.26	0.31	0.29	0.33

(b) *x*-axis-parallel profiles

Surface	*x*-axis-parallel profiles (Face 1-Face 3)										
	y=0 mm	y=20 mm	y=40 mm	y=60 mm	y=80 mm	y=100 mm	y=120 mm	y=140 mm	y=160 mm	y=180 mm	y=200 mm
Upper	0.25	0.26	0.51	0.23	0.23	0.20	0.22	0.67	0.27	0.49	0.29
Lower	0.25	0.26	0.51	0.23	0.23	0.20	0.22	0.67	0.27	0.49	0.29

(c) Maximum, minimum, mean value and standard deviation of Z_2

Surface	*y*-axis parallel profiles (Face 2-Face 4)					*x*-axis parallel profiles (Face 1-Face 3)				
	Max.	Min.	Mean	Stdev	COV(%)	Max.	Min.	Mean	Stdev	COV(%)
Upper	0.35	0.25	0.29	0.02	7	0.67	0.2	0.33	0.15	45
Lower	0.49	0.25	0.31	0.06	19	0.67	0.2	0.33	0.15	45

4.1.2 Mechanical model and aperture field

The calibration results of the mechanical model are presented in Figure 4-3. The applied stress ranges from 0 to 40 MPa. The initial contact state is established by aligning the point clouds of the upper and lower fracture surfaces using the ICP algorithm, followed by a 0.05 mm upward translation of the upper surface in the *z*-axis direction, resulting in a separation between the surfaces. The Young's modulus is set to 73 GPa, which is similar to the average value of each test in Table 2-5.

Figure 4-3 shows a comparison of the variation in average aperture obtained from the mechanical model under each stress state and the changes measured by the LVDTs in the experiment (Table 2-2 ~ 2-4). Although the simulated displacement results are generally greater than those of the "unopened" specimen with flow direction from Face 1 to Face 3, and generally smaller than those of the "resealed" specimen with flow direction from Face 2 to Face 4, the simulation results fall approximately at the average of all displacement data in the loading range of 0–8 MPa. In the loading range of 8–40 MPa, the simulated trend closely resembles that of the "resealed" specimen with flow direction from Face 2 to Face 4.

Table 4-4 summarizes the contact ratio, average aperture, and 99th percentile aperture values at each loading stage. Figure 4-4 shows the aperture fields for this 200 x 200 mm^2 fracture of initial state and with normal loading 40 MPa, where the overall reduction in the aperture field can be observed. The contact zones of the upper and lower fracture surfaces are similar to the pressure film results shown in Figure 2-16. Figure 4-5 presents the histogram of aperture values corresponding to the data shown in Figure 4-4.

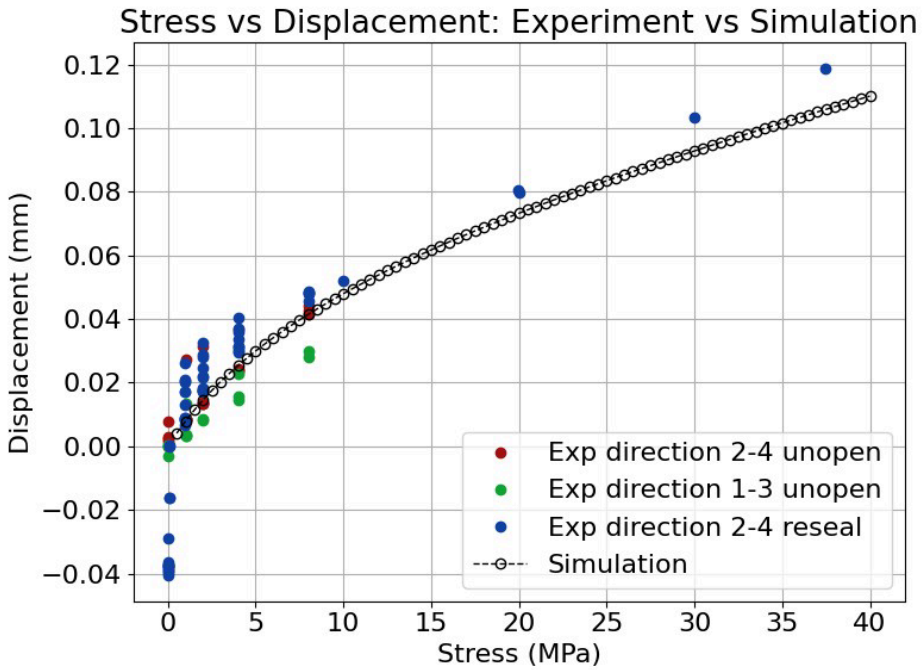

Figure 4-3. *Comparison of the average displacement at different loading stage between experimental and numerical results. Displacement was computed by selecting one LVDT measurement as a reference point, with the displacements of the remaining LVDT readings calculated as the differences relative to this reference. Specifically, for the cases of "Exp direction 2-4 unopen," "Exp direction 1-3 unopen," and "Exp direction 2-4 reseal," the first entry from Table 2-2, the first entry from Table 2-3, and the 52nd entry from Table 2-4 were used as reference values, respectively.*

Table 4-4. Simulated variation of aperture for 200x200 mm^2 fracture with different normal loading

Stress (MPa)	Contact Ratio (%)	Mean Aperture (mm)	99th Aperture (mm)
0.0	17	6.0E-02	8.1E-01
1.0	20	5.4E-02	8.0E-01
2.0	24	4.9E-02	8.0E-01
4.0	31	4.1E-02	7.9E-01
8.0	42	3.0E-02	7.7E-01
10.0	47	2.7E-02	7.6E-01
20.0	67	1.6E-02	7.4E-01
30.0	79	1.0E-02	7.2E-01
37.5	85	7.9E-03	7.1E-01
40.0	86	7.3E-03	7.0E-01

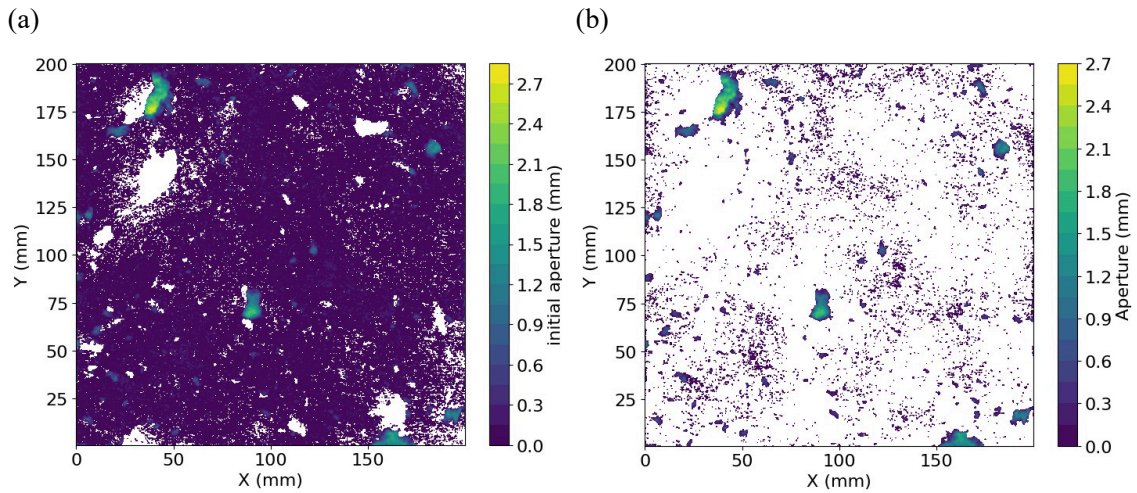

Figure 4-4. *Aperture fields of 200x200 mm^2 fracture of (a) initial state, and (b) under 40 MPa normal loading.*

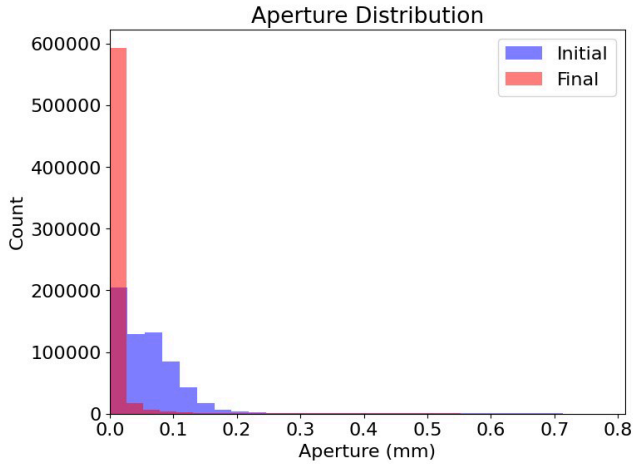

Figure 4-5. *Statistical histogram of aperture for 200 x 200 mm^2 of initial state (0 MPa) and final state (40 MPa).*

4.1.3 Uncertainty Analysis of mechanical model

The uncertainty analysis of the mechanical model primarily focuses on the initial contact state settings and the corresponding calibration results of Young's modulus. After applying the ICP algorithm to align the fracture surfaces, three cases were analysed: (1) no translation, (2) a *z*-axis direction translation of 0.05 mm, and (3) a *z*-axis direction translation of 0.1 mm. These 3 cases correspond to calibrated Young's moduli of 50 GPa, 73 GPa, and 100 GPa, respectively, in order to fit the experimental data.

Among the three, the second case, *z*-axis direction translation of 0.05 mm, produced a simulated displacement curve that closely matches the central trend of all experimental data (Figure 4-3). The associated Young's modulus also aligns well with the experimental results (Table 2-5), and thus this case is used as the primary scenario for further analysis. The first and third cases yield simulated displacement curves that generally represent the lower (Figure 4-6 (a)) and upper (Figure 4-6 (b)) bounds of the experimental data, respectively. These cases are further examined in Section 4.2.2 to assess the impact of varying initial contact conditions on the uncertainty in the hydraulic model.

(a)

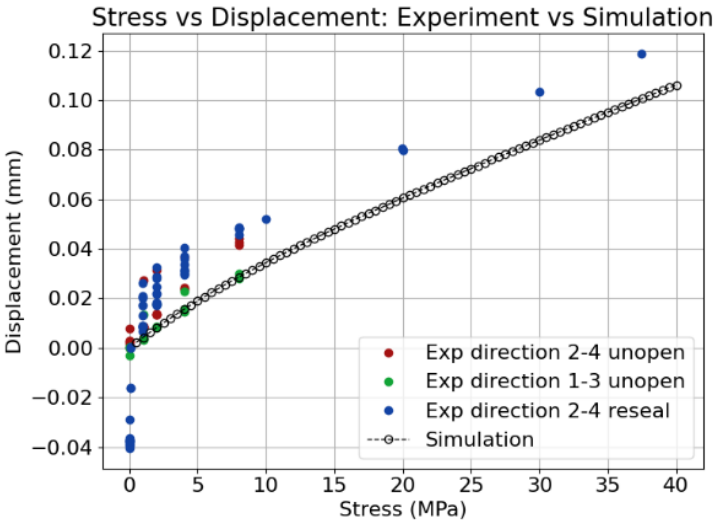

(b)

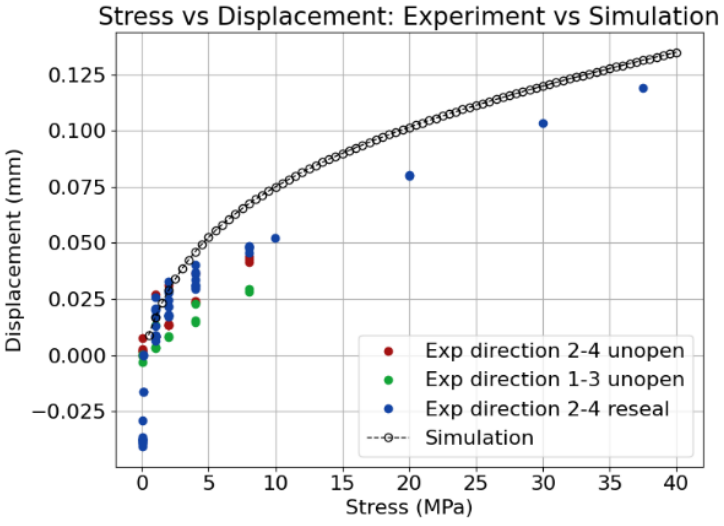

Figure 4-6. *Comparison of experimental and simulated stress-displacement curves for (a) the no-translation case and (b) the 0.1 mm z-axis direction translation case.*

4.2 Water flow prediction

4.2.1 Flow rate prediction under various normal loads

Figure 4-7 presents the simulated hydraulic head fields under loading conditions of 0 MPa and 40 MPa, along with flow paths visualized using velocity vectors superimposed on the aperture fields. The results demonstrate that this simulation approach effectively captures the tendency of flow to concentrate in regions with larger apertures (denser streamlines) and to avoid regions with smaller apertures (sparser streamlines). Consequently, the hydraulic head contours exhibit localized variations in density. However, as the applied stress increases and most of the fracture closes, the degree of streamline curvature and the variability in hydraulic head contour spacing become significantly less obvious.

Figure 4-8 presents a comparison between the simulated results and experimental data, based on the aperture fields derived from the mechanical simulation results shown in Figure 4-3. To facilitate comparison, the flow rate is normalized by the hydraulic gradient and the outlet boundary size of the specimen to obtain the equivalent transmissivity. Figure 4-8 shows that the variation in equivalent transmissivity follows a consistent decreasing trend with increasing normal stress in both the simulation and the experimental data.

The numerical simulations yield nearly identical results for both flow directions (Face 1–Face 3 and Face 2–Face 4), indicating that the current modelling approach failed to capture flow anisotropy. However, experimental data show that during the Face 2–Face 4 flow tests on the resealed specimen, the data range at each stress state in the 0–8 MPa cyclic loading process contains the results obtained from the unopen specimen tested in the Face 1–Face 3 flow direction. This suggests that slight variations in hydraulic behaviour may arise due to minor changes in the contact condition during the application or removal of water pressure or mechanical loading throughout the experiment. Nonetheless, we believe that anisotropy is still present, as suggested by the flow test results. Specifically, the measured flow rates from the Face 1–Face 3 direction in the unopened specimen are consistently lower than those from the Face 2–Face 4 direction in the same specimen.

4.2.2 Uncertainty analysis of hydraulic model

To build upon the analyses presented in Sections 4.1.3 and 4.2.1, the uncertainty analysis of the hydraulic model was conducted using aperture fields derived from three distinct initial contact states considered in the mechanical simulations of Section 4.1.3. This analysis aims to investigate the potential hydraulic responses associated with varying initial mechanical conditions during the loading process.

The resulting stress-equivalent transmissivity curves exhibit a consistent decreasing trend and successfully contain the range of experimental measurements (Figure 4-9). This suggests that the assumed variation in initial contact states sufficiently accounts for the observed variability in fracture transmissivity.

4.2.3 Minimum Transmissivity

To estimate the potential lower bound of fracture transmissivity, we set the minimum hydraulic aperture to 1e-3, 3e-3, and 5e-3 mm, corresponding to transmissivity values of 8e-13, 2e-11, and 1e-10 m^2/s, respectively. Figure 4-10 presents a comparison between the simulated results under these assumptions and the experimental data. The results indicate that prior to 10 MPa, the simulated equivalent transmissivity values are similar across different assumptions. However, beyond 10 MPa, the equivalent transmissivity tends to converge toward the assigned minimum transmissivity values. This behaviour arises because the contact ratio exceeds 50% after 10 MPa, causing the transmissivity of the closed regions to dominate the simulation outcome. Assuming the mechanical model is valid, this suggests that even when the fracture is nominally closed, flow paths in micro-scale may still exist, resulting in a non-zero minimum transmissivity. Based on the simulation results, we infer that the possible lower bound of fracture transmissivity is approximately 2e-11 m^2/s.

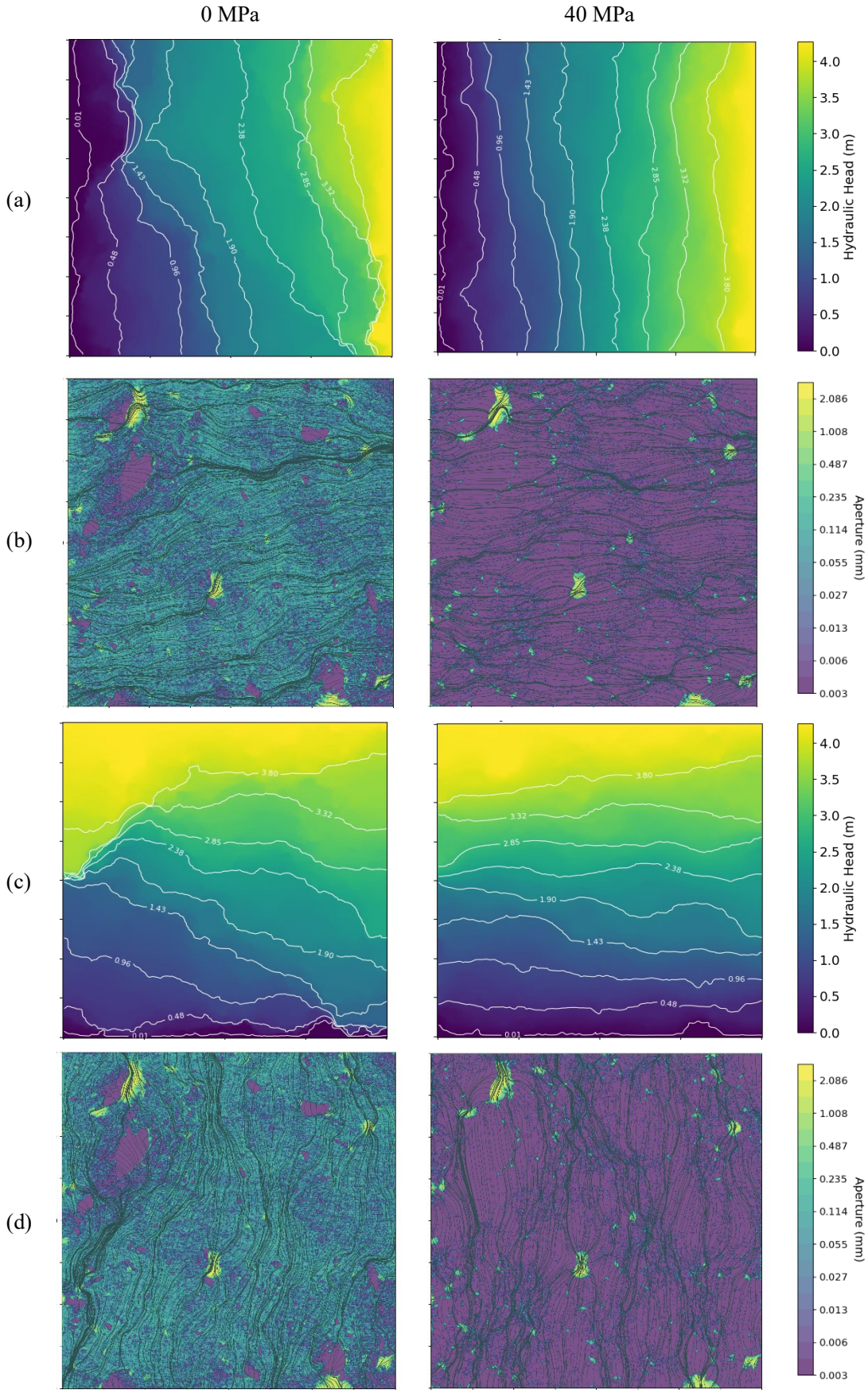

Figure 4-7. *Steady-state simulation results. (a) Head fields of flow from Face 1 to Face 3, (b) streamlines of flow from Face 1 to Face 3 superimposed on aperture fields, (c) Head fields of flow from Face 2 to Face 4, (d) streamlines of flow from Face 2 to Face 4 superimposed on the aperture fields.*

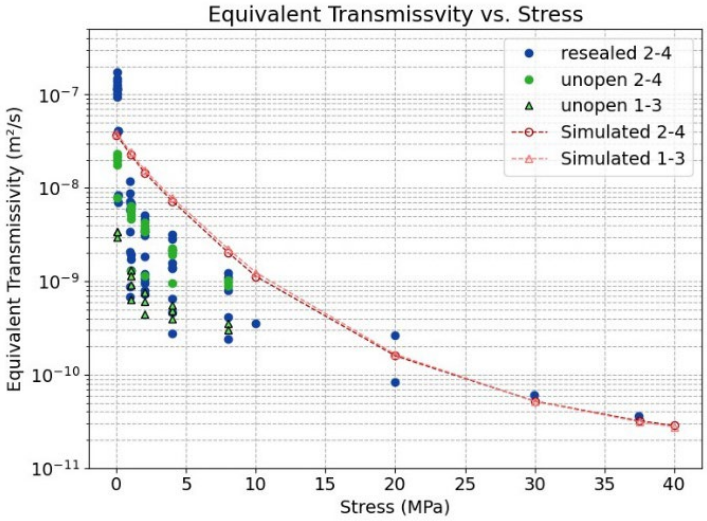

Figure 4-8. *Comparison of transmissivity results of flow direction 1-3 and 2-4 between experimental and numerical results.*

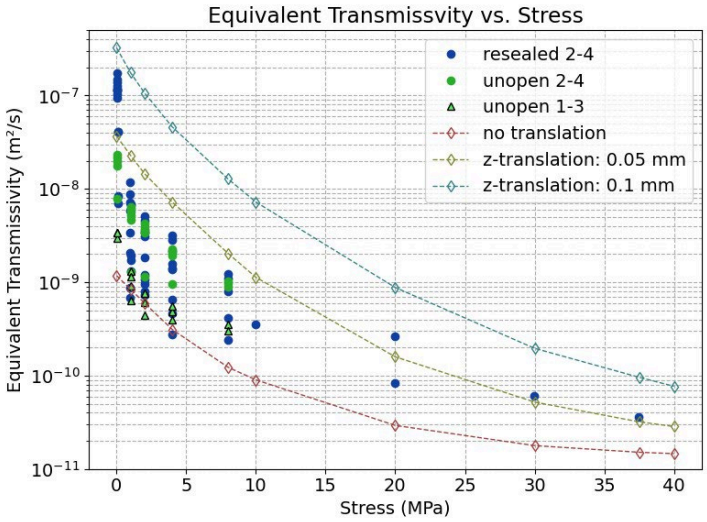

Figure 4-9. *Equivalent transmissivity versus normal stress under different initial contact assumptions.*

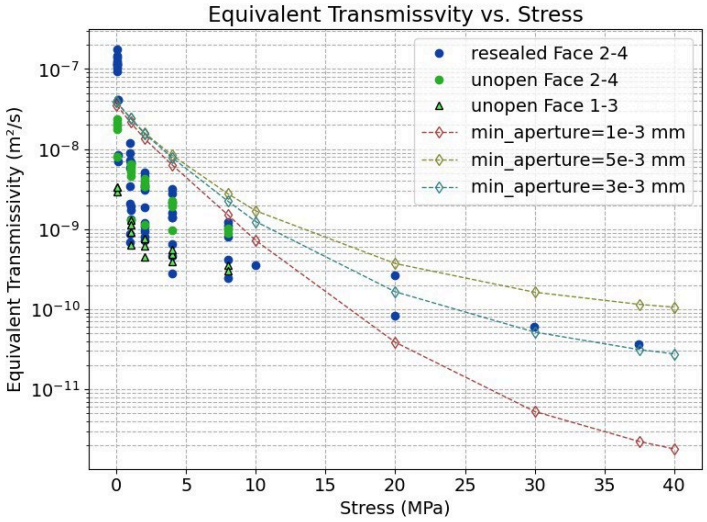

Figure 4-10. *Equivalent transmissivity versus normal stress under different minimum transmissivity.*

4.2.4 Channelling effect under various normal loads

Figures 4-11 show the flow rate fields for the flow directions from Face 1 to Face 3 and from Face 2 to Face 4 under the 0 MPa, 8 MPa, and 20 MPa normal loading conditions.

The results indicate that as normal stress increases, the flow becomes increasingly concentrated. This flow concentration trend can be quantitatively characterized using the channelling factor, d_{qnet}. Figure 4-12 summarizes the decreasing trend of d_{qnet} with increasing normal stress for different flow directions, along with the normalized flow rate difference ($\frac{Q_{max}-Q_{min}}{Q_{mean}}$) at each stress state. The findings show that as the degree of closure increases, the overall flow rate decreases, while the disparity between the maximum and minimum flow rates becomes more pronounced. The normalized flow rate difference decreases with high stress because the fracture becomes highly closed overall, and the remaining regions with relatively larger apertures continue to close, which further reduces flow concentration.

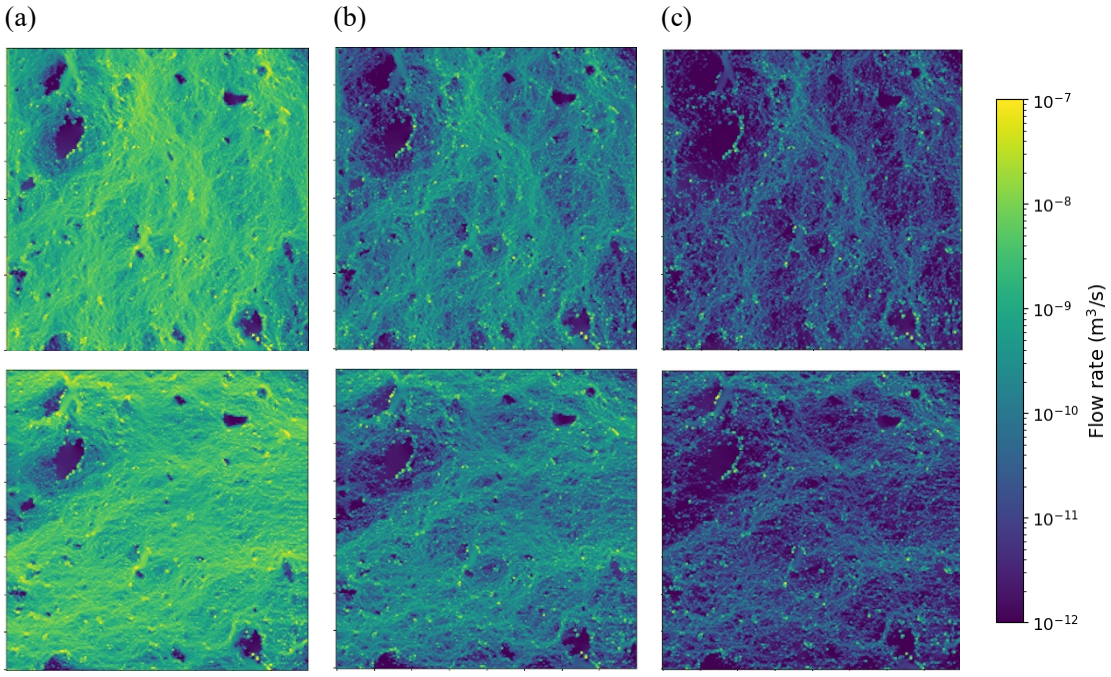

Figure 4-11. *Flow rate fields used to calculate channelling factor. (a) 0 MPa; (b) 8 MPa; (c) 20 MPa.*

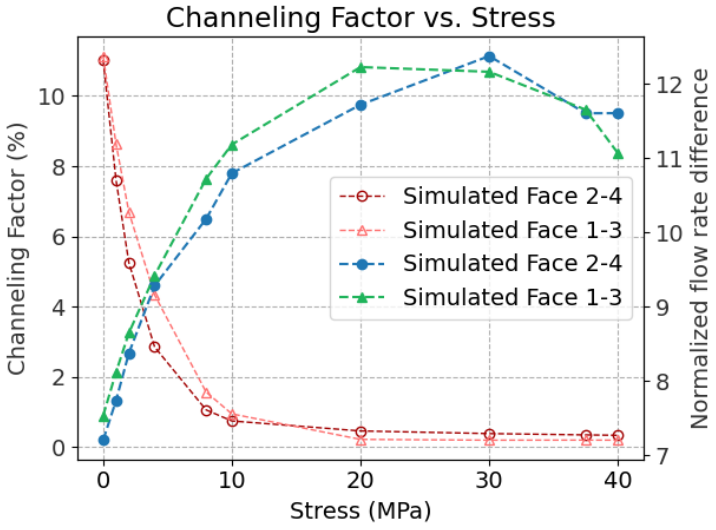

Figure 4-12. *Comparison of channelling factor simulation results under different loading stresses with flow direction from Face 1 to Face 3 and from Face 2 to Face 4.*

5 Discussion, summary, and conclusions

5.1 Discussion

The primary modelling goal of this study was to predict how a fracture's transmissivity and flow rate change under varying normal stresses. This goal has been achieved, and the following is the further statement. The integrated hydro-mechanical simulation reproduced the stress-dependent hydraulic behaviour of the fracture and captured the observed trend of decreasing equivalent transmissivity with increasing normal load. The resulting flow predictions for different normal stresses showed good agreement with experimental measurements.

(1) Key Assumptions and Justifications

- **Rigid Alignment and Initial Contact:** The ICP alignment provided a first-order approximation of the mating between the rough surfaces, given that the true initial contact configuration was unknown. By adjusting the *z*-axis direction translation, different possible initial contact states were simulated, reflecting uncertainty in how the fracture might be aligned naturally or during the experiment.
- **Elastic Deformation of Asperities:** Under normal loading, the fracture was assumed to deform purely elastically, without permanent damage. The normal closure behaviour was calibrated to match the LVDT displacement-load curves by adjusting an effective Young's modulus.
- **Aperture-Based Transmissivity via Cubic Law:** The aperture field computed from the elevation difference of fracture surfaces at each loading stage was converted to a transmissivity field using the cubic law. Laminar flow through the fracture was assumed. The cubic law is a classic and physically based approximation for flow between parallel plates.

(2) Key Uncertainty and Limitation

- **Initial Contact Configuration:** The true initial contact zones and aperture fields are not directly measurable. Different possible alignments of the fracture surfaces could exist, especially since each aligned state might be different slightly when conducting each experiment because of moving or loading on the specimen. This introduces uncertainty in the initial aperture field. In our model, the ICP alignment and assumed initial contact state are an approximation. As a result, initial contact states could yield different aperture fields and outcomes of flow simulation. We partially addressed this by treating the magnitude of *z*-axis direction translation as a variable and observing the effect on predictions providing a range of equivalent transmissivity outcomes.
- **Residual Flow in Contact Zones:** Regions where the mechanical model predicted zero or near-zero aperture were assigned a very small but non-zero transmissivity value. This reflects the reality that even closed contacts might permit some flow in micro-scale along asperity edge or through local micro-cracks. By assigning minimum transmissivity value for contact zones, we acknowledge this micro-flow and ensure the model's stability.
- **Material Homogeneity:** We assumed a uniform elastic modulus for the rock and identical mechanical behaviour at all contact zones. However, natural fractures may exhibit spatial variability in stiffness due to rock heterogeneity or differences in asperity hardness. Such heterogeneity was not considered in the mechanical model. This assumption may result in inaccurate estimations of fracture closure behaviour, particularly under high normal stresses, where incomplete closure may persist due to mismatched hardness between opposing asperities.

(3) Data Quality and Resolution

The quality and resolution of input data in this study were generally high, enabling a detailed modelling approach. The fracture surfaces were characterized by point clouds from high-resolution scanning. It allowed the model to identify detailed contact zones and aperture fields. If the scans had been significantly coarser, many small-scale asperity contacts and void would have been missed, greatly increasing uncertainty in the flow simulation.

The quality of loading data was also high. 4 LVDTs recorded the closure of the fracture during applying normal stress, yielding precise displacement curves. These curves were directly used to calibrate the elastic mechanical model, essentially anchoring the simulation to observed mechanical behaviours. The contact model could not have been confidently tuned without displacement measurements at each loading stage.

In addition to the mechanical data, the flow rate measurements obtained from the constant head experiments were also of high quality. These data provided reliable values of flow rate under various loading conditions and were essential for model validation.

(4) Assessment of Confidence

Given the careful calibration and the consistency between predictions and measurements, we have moderate to high confidence in the model's predictive capability within the scope of this study. The model's ability to approximate experimental flow rates under various stress conditions strongly indicates its validity and suggests that the governing physics, elastic mechanics and the cubic law, are properly captured. We consider the predictions to be reliable for the tested conditions, specifically for the fracture under normal stresses up to 40 MPa and steady-state flow under a head gradient.

However, certain ambiguities remain in this study, which limit our confidence in the model's predictive capabilities. In the uncertainty analysis, both mechanical and hydraulic models were simulated by varying the initial contact states. The resulting distributions of the displacement–stress and equivalent transmissivity–stress curves were able to capture the variability observed in the experimental data. While these results indicate a certain degree of model applicability, the underlying causes of the observed variability have not been thoroughly investigated.

(5) Model Improvement

- **Advanced Contact Mechanics:** Future models could incorporate non-linear or plastic deformation behaviours for asperities. Besides, considering heterogeneity in contact stiffness, e.g. a spatial distribution of Young's modulus or hardness for different contact zones, could capture the progressive closure of softer asperities before harder ones.
- **Hydraulic Model Refinement:** The hydraulic model could be refined to account for flow tortuosity and anisotropy. In this study, we observed slightly different equivalent transmissivities in two orthogonal directions, flow from Face 1 to Face 3 vs from Face 2 to Face 4, might due to the anisotropy of the surface geometry.
- **Upscaling Analysis:** In practice, the available information on fractures is often limited or partial, such as small-scale fracture surfaces obtained from borehole samples or fracture traces observed on outcrops or tunnel walls. Such upscaling analysis can enhance confidence in extrapolating the mechanical and hydraulic properties of fractures from laboratory-scale specimens to larger-scale geological features.

5.2 Summary

In Task 10.2.2, the provided HM coupling experiment data is highly detailed. This experiment utilized a 200 x 200 mm² fracture specimen to conduct constant head tests in different directions, with the application of normal stress to observe the effect of normal closure on fracture transmissivity. To understand the relationship between fracture surface geometry and transmissivity, high-precision scanning is used to obtain point cloud data of the fracture surface. The NTU modelling team has developed a modelling process that utilizes HM test data to visualize the potential head fields, predict the flow rates and equivalent transmissivity in different flow directions corresponding to various loading, and observe the impact of stress on the channelling effect.

The modelling process follows a one-way HM coupling approach, where the mechanical model is first used to obtain the aperture fields under different loading states and then estimate the corresponding transmissivity.

This study adopted the method shown in Figure 3-1, import the aligned fracture surfaces into the mechanical contact model to obtain aperture fields under various stress conditions, from which transmissivity fields were calculated.

A hydraulic model was then used to simulate the hydraulic head fields, along with flow rates and corresponding equivalent transmissivity values in two flow directions in the fracture. The results revealed a clear trend, that is the overall equivalent transmissivity declined significantly as the normal stress increased from 0 to 40 MPa. This trend aligned well with experiment measurements, confirming the reduction in fracture transmissivity under loading conditions.

A channelling factor analysis revealed that flow heterogeneity increased with increasing fracture closure, consistent with the expectation that higher normal stress promotes flow concentration in regions with relatively larger apertures. However, at the higher stress levels, the fracture became mostly closed that the overall degree of flow localization slightly decreased, due to the continuous reduction of open zones.

Overall, the study successfully employed a calibrated model, based on high-resolution fracture surface profiles and displacement data under loading, to predict flow behaviours at different stress levels. It also provided insights into the channelling effect on rough fracture surfaces. Moreover, uncertainty analyses were conducted using varying initial contact states, and the predicted results captured the variability observed in experimental data. These outcomes enhance confidence in the methodology of inferring hydraulic behaviours from mechanical data.

5.3 Conclusions

- **Achievement of Modelling Goals:** The study successfully achieved its modelling objectives by predicting the fracture's hydraulic behaviour under varying normal stresses. The simulated equivalent transmissivity vs. normal stress relationship closely fit the experimental trend, capturing the reduction in flow rate as stress increased, indicating that the model can reliably reproduce observed phenomena.
- **Pragmatic Validation:** A key outcome of this study is that the model was successfully validated through a prediction outcome exercise. The model was calibrated using displacement data from the mechanical tests, and the predicted flow rates, which is calculated into equivalent transmissivity, were then compared against experimental measurements. This clear separation between the calibration data and the validation data allowed for a meaningful test of the model's predictive ability. The fact that the experimental flow rates fell within the range predicted by the model supports the reliability of the modelling approach and the parameter choices.
- **Hydro-Mechanical Insights:** The findings of this study reinforce fundamental understanding of fracture flow under applied stress. Experimental results, in which normal stresses ranging from 0 to 40 MPa were applied to fracture specimens, demonstrate that fracture closure significantly results in the reduction of transmissivity. This stress range approximately corresponds to in-situ stress conditions at depths up to 1500 meters. Understanding how transmissivity is affected within this stress range provides valuable insights for analysing stress-induced transmissivity changes in underground rock engineering applications.

References

SKB's (Svensk Kärnbränslehantering AB) publications can be found at www.skb.com/publications.

Barton N, Choubey V, 1977. The shear strength of rock joints in theory and practice. Rock Mechanics 10: 1-54.

Besl P J, McKay N D, 1992. Method for registration of 3-D shapes. In Sensor fusion IV: control paradigms and data structures. 1611, 586-606.

Lanyon G W, Davy P, Dershowitz W S, Finsterle S, Gylling B, Hyman J D, Neretnieks I, Uchida M, 2021. Pragmatic Validation Approach for Geomechanics, Flow, and Transport Models in Fractured Rock Masses. Paper (DFNE 21-2369) presented at the 3rd International Discrete Fracture Network Engineering Conference, Virtual, June 2021.

Maillot J, Davy P, le Goc R, Darcel C, de Dreuzy J R, 2016, Connectivity, permeability, and channeling in randomly distributed and kinematically defined discrete fracture network models. Water Resour. Res. 52:8526–8545.

Tatone BSA, Grasselli G, 2009. A method to evaluate the three-dimensional roughness of fracture surfaces in brittle geomaterials. Rev Sci Instrum 80:125110.

Yu X, Vayssade B, 1991. Joint profiles and their roughness parameters. Int J Rock Mech Min 28:333–336.